

Diagrammatic Monte Carlo Method for Impurity Models with General Interactions and Hybridizations

Jia Li,¹ Markus Wallerberger,^{1,2} and Emanuel Gull¹

¹*Department of Physics, University of Michigan, Ann Arbor, MI 48109, USA*

²*Institute of Solid State Physics, Vienna University of Technology, A-1040 Vienna, Austria*

(Dated: July 27, 2020)

We present a diagrammatic Monte Carlo method for quantum impurity problems with general interactions and general hybridization functions. Our method uses a recursive determinant scheme to sample diagrams for the scattering amplitude. Unlike in other methods for general impurity problems, an approximation of the continuous hybridization function by a finite number of bath states is not needed, and accessing low temperature does not incur an exponential cost. We test the method for the example of molecular systems, where we systematically vary temperature, interatomic distance, and basis set size. We further apply the method to an impurity problem generated by a self-energy embedding calculation of correlated antiferromagnetic NiO. We find that the method is ideal for quantum impurity problems with a large number of orbitals but only moderate correlations.

I. INTRODUCTION

Quantum impurity models, originally introduced to describe magnetic impurities such as iron or copper atoms with partially filled d-shells in a non-magnetic host material [1], have since found applications in nanoscience as representations of quantum dots and molecular conductors [2], and in surface science to understand the adsorption of atoms on surfaces [3, 4]. In addition, they form the central part of embedding theories such as the dynamical mean field theory (DMFT) [5, 6] and its variants [7–19], as well as the self-energy embedding theory (SEET) [20–22], where they describe the behavior of a few ‘strongly correlated’ orbitals embedded into a weakly correlated or non-interacting background of other orbitals. These methods promise a systematic route for the simulation of strongly correlated quantum many-body problems [23].

While the original formulation of a quantum impurity model [1] only describes a single correlated orbital coupled to a non-interacting environment, in general the impurities occurring in the context of surface science and embedding theories contain many orbitals with general four-fermion interactions and few symmetries [24]. The time-dependent hybridization function describing the hopping between the impurity and its environment is typically such that it cannot be diagonalized for all frequencies at once.

Solving quantum impurity problems, i.e. obtaining the impurity Green’s function given an impurity Hamiltonian and a hybridization function, requires the use of numerical methods. A wide range of such methods exist. Hamiltonian-based methods, such as exact diagonalization [25–29] and its variants [30], configuration-interactions [31], or coupled cluster theory [32, 33], solve the impurity problem by mapping the impurity problem onto a system with a local Hamiltonian and a finite number of auxiliary ‘bath’ states chosen to fit the time-dependent hybridization function. The methods are limited to a relatively small set of strongly interacting sites or break down at moderate correlation strength.

The bath fitting, which typically approximates a continuous bath dispersion by a non-linear fit to a small number of delta-function peaks, introduces additional approximations [27, 29]. Numerical renormalization techniques [34, 35] overcome this issue by providing an almost continuous bath density of states but are in turn limited to a few orbitals in highly symmetrical situations.

A complementary approach is given by Monte Carlo techniques such as the continuous-time quantum Monte Carlo methods [36]. These methods are based on a stochastic sampling of the terms in a diagrammatic expansion of the partition function. For particle-hole symmetric systems with on-site density-density interactions, interaction expansion methods [37–39] can solve systems with hundreds of strongly correlated orbitals [40]. Away from particle hole symmetry and at low temperature, they are typically limited to around eight orbitals, and their naive adaptation to general four-fermion operator terms suffers from a severe sign problem [41]. In contrast, a partition function expansion in the hybridization [42–44] is able to work with general local Hamiltonians of up to five orbitals, but is similarly restricted to diagonal hybridization functions. A reformulation [45] in terms of ‘inchworm’ diagrams [46] overcomes the restriction of diagonal hybridizations, but so far remains limited to impurities with up to three orbitals.

There is therefore a need for impurity solver methods that can treat the problems of embedding theory and surface science, where several orbitals with general interactions and hybridizations occur. Diagrammatic Monte Carlo methods [47–51], which expand physical observables rather than partition functions, along with efficient ways of evaluating the resulting diagrammatic series via the connected determinant (CDet) approach [52–57], are promising. While these methods suffer from other limitations, including divergences of the series in the strong correlation regime, they do not require to approximate the hybridization function by a fit, and are not based on a diagonalization of the local Hamiltonian.

In this paper, we show a formulation of the diagram-

matic Monte Carlo method for impurity problems with general interactions and hybridizations based on the CDet framework. We test the method on the example of molecular systems, for which a broad range of very mature Hamiltonian methods exist. From the point of view of the algorithmic formulation, the molecular systems exhibit the full complexity of general impurity problems. The only difference between molecules and quantum impurities is that the latter are formulated with a time-dependent hybridization, rather than an instantaneous hopping. This hybridization function modifies the bare propagator but otherwise leaves the system and our algorithmic approach invariant. Applications to molecular systems therefore form an ideal testbed for impurity solver methods of this type. We complete our benchmark by applying the impurity solver to an impurity generated by a self-energy embedding calculation of antiferromagnetic solid NiO [58].

We carefully analyze the convergence behavior of the diagrammatic expansion and the computational cost of the method as a function of varying temperature, basis sets, intermolecular distance, and system size. We emphasize that we do not intend to present our method as a viable method for quantum chemistry systems without retardation effects. Rather, we exploit the rigorous and controlled framework of molecular simulations to generate a series of test cases that illustrate various parameter regimes in quantum impurities.

This paper will proceed as follows. In Sec. II we introduce the computational problem, the diagrammatic formulation, and the algorithmic description. In Sec. III we present applications to molecular systems and benchmark results for quantum impurities. Finally, Sec. IV presents conclusions. Appendices A through E present technical details useful for implementing our algorithm and reproducing our results.

II. METHOD

A. Partition function expansion

We describe molecular electrons using the following Hamiltonian:

$$\hat{H} = \underbrace{\sum_{ab} h_{ab} \hat{c}_a^\dagger \hat{c}_b}_{\hat{H}_0} + \underbrace{\frac{1}{4} \sum_{abcd} U_{abcd} \hat{c}_a^\dagger \hat{c}_c^\dagger \hat{c}_d \hat{c}_b}_{\hat{H}_V}, \quad (1)$$

where a, b, c, d denote spin-orbitals, $1, \dots, N$. We employ second quantization: \hat{c}_a and \hat{c}_a^\dagger annihilates and creates, respectively, an electron in the spin-orbital a . The non-interacting term \hat{H}_0 is parametrized by the one-electron integrals $h_{ab} = [a|h|b]$, whereas the interacting term \hat{H}_V is parametrized by the antisymmetrized two-electron integrals $U_{abcd} = [ab|cd] - [ad|cb]$. We note that explicit antisymmetrization, $U_{abcd} = -U_{adcb} = U_{cdab}$, avoids ambiguities in the diagrammatic expansions below [59]. We

orthonormalize the basis, $\{\hat{c}_a^\dagger, \hat{c}_b\} = \delta_{ab}$, as we empirically found this to improve the error bars in the subsequent Monte Carlo procedure. For completeness, we compiled the explicit expressions for h and U in Appendix A.

As we are going to perform series expansions later, it is convenient to introduce an expansion parameter ξ into the Hamiltonian:

$$\hat{H}_\xi = \hat{H}_0 + \xi \hat{H}_V. \quad (2)$$

The non-interacting case is given by $\hat{H}_{\xi=0}$, whereas $\hat{H}_{\xi=1}$ recovers the full Hamiltonian (1).

We are primarily interested in calculating finite temperature observables such as energies, densities, as well as the spectral function and other electronic correlation functions. We start with the grand-canonical partition function:

$$Z_\xi = \text{Tr} \exp[-\beta(\hat{H}_\xi - \mu \hat{N})], \quad (3)$$

where $\beta = 1/T$ is the inverse temperature, μ denotes the chemical potential, and $\hat{N} = \sum_a \hat{c}_a^\dagger \hat{c}_a$ is the density operator. Expanding Eq. (3) about $\xi = 0$ within the interaction picture [60] yields the Dyson series:

$$Z_\xi = Z_0 \sum_{k=0}^{\infty} \frac{(-\xi)^k}{k!} \int_0^\beta d^k \tau \langle \hat{H}_V(\tau_1) \cdots \hat{H}_V(\tau_k) \rangle_0, \quad (4)$$

where $Z_0 := \text{Tr} \exp[-\beta(\hat{H}_0 - \mu \hat{N})]$ is the non-interacting partition function, τ denotes imaginary (Euclidean) time, $\langle \cdot \rangle_0$ denotes the non-interacting expectation value:

$$\langle \hat{X}_1 \cdots \hat{X}_k \rangle_0 := \frac{1}{Z_0} \text{Tr} [e^{-\beta(\hat{H}_0 - \mu \hat{N})} \mathcal{T}(\hat{X}_1 \cdots \hat{X}_k)], \quad (5)$$

and \mathcal{T} indicates path ordering in imaginary time. We note that for molecules, both \hat{H}_0 and \hat{H}_V are bounded and thus away from zero temperature, the series expansion for the partition function (4) is absolutely convergent for all ξ .

Inserting Eq. (1) into Eq. (4) yields:

$$\begin{aligned} \frac{Z_\xi}{Z_0} &= \sum_{k=0}^{\infty} \frac{(-\xi)^k}{k!} \sum_{a_1 b_1 c_1 d_1} \cdots \sum_{a_k b_k c_k d_k} \int_0^\beta d\tau_1 \cdots \int_0^\beta d\tau_k \\ &\times \left(\frac{U_{a_1 b_1 c_1 d_1}}{4} \right) \cdots \left(\frac{U_{a_k b_k c_k d_k}}{4} \right) \langle \hat{c}_{a_1}^\dagger(\tau_1) \hat{c}_{c_1}^\dagger(\tau_1) \\ &\times \hat{c}_{d_1}(\tau_1) \hat{c}_{b_1}(\tau_1) \cdots \hat{c}_{a_k}^\dagger(\tau_k) \hat{c}_{c_k}^\dagger(\tau_k) \hat{c}_{d_k}(\tau_k) \hat{c}_{b_k}(\tau_k) \rangle_0. \end{aligned} \quad (6)$$

In order to simplify our notation we combine four spin-orbitals a, b, c, d and an imaginary time τ into a single “vertex” $v = (a_v, b_v, c_v, d_v, \tau_v)$. We also introduce the

following shorthands:

$$\int d^k \mathcal{V} := \frac{1}{k!} \prod_{v \in \mathcal{V}} \sum_{a_v b_v c_v d_v} \int_0^\beta d\tau_v \quad (7a)$$

$$D(\mathcal{V}) := \prod_{v \in \mathcal{V}} \left(-\frac{U_{a_v b_v c_v d_v}}{4} \right) \times \left\langle \prod_{v \in \mathcal{V}} \hat{c}_{a_v}^\dagger(\tau_v) \hat{c}_{c_v}^\dagger(\tau_v) \hat{c}_{d_v}(\tau_v) \hat{c}_{b_v}(\tau_v) \right\rangle_0. \quad (7b)$$

Eq. (7b) emphasizes the fact that expectation value in Eq. (6) corresponds to the sum over all disconnected and connected Feynman diagrams with vertices $\mathcal{V} = (v_1, \dots, v_k)$, while Eq. (7a) just corresponds to the sum over all internal degrees of freedom of the diagrams. With these substitutions, Eq. (6) simplifies to:

$$\frac{Z_\xi}{Z_0} = \sum_{k=0}^{\infty} \xi^k \int d^k \mathcal{V} D(\mathcal{V}). \quad (8)$$

To evaluate Eq. (8), we first introduce the non-interacting Green's function:

$$g_{ba}(\tau) = -\langle \hat{c}_b(\tau) \hat{c}_a^\dagger(0) \rangle_0 = [(-\partial_\tau + \mu)\mathbf{1} - h]_{ba}^{-1}. \quad (9)$$

Given a diagram $\mathcal{V} = (v_1, \dots, v_k)$ with $v_i = (a_i, b_i, c_i, d_i, \tau_i)$, we can use Wick's theorem to write Eq. (7b) as:

$$D(\mathcal{V}) = \prod_{i=1}^k \left(-\frac{U_{a_i b_i c_i d_i}}{4} \right) \det \mathbf{G}(\mathcal{V}), \quad (10)$$

where \mathbf{G} is a $2k \times 2k$ matrix in which the rows (columns) correspond to the $2k$ annihilation (creation) operators. Introducing the column and row indices α, β, \dots such that

$$\begin{aligned} \{a_\alpha\} &:= \{a_1, c_1, a_2, c_2, \dots, a_k, c_k\}, \\ \{b_\beta\} &:= \{b_1, d_1, b_2, d_2, \dots, b_k, d_k\}, \\ \{\tau_\alpha\} &= \{\tau_\beta\} := \{\tau_1, \tau_1, \tau_2, \tau_2, \dots, \tau_k, \tau_k\}, \end{aligned} \quad (11)$$

we define the matrix elements

$$\begin{aligned} [\mathbf{G}(\mathcal{V})]_{\beta\alpha} &:= -\langle \hat{c}_{b_\beta}(\tau_\beta) \hat{c}_{a_\alpha}^\dagger(\tau_\alpha) \rangle_0 \\ &= g_{b_\beta a_\alpha}(\tau_\beta - \tau_\alpha + 0^-). \end{aligned} \quad (12)$$

The full matrix can be written in a block form as

$$\mathbf{G}(\mathcal{V}) := \begin{bmatrix} \mathbf{g}_{11} & \mathbf{g}_{12} & \cdots & \mathbf{g}_{1n} \\ \mathbf{g}_{21} & \mathbf{g}_{22} & \cdots & \mathbf{g}_{2n} \\ \vdots & \vdots & \ddots & \vdots \\ \mathbf{g}_{n1} & \mathbf{g}_{n2} & \cdots & \mathbf{g}_{nn} \end{bmatrix}, \quad (13)$$

where each 2×2 block is given by

$$\mathbf{g}_{ij} := \begin{bmatrix} g_{b_i a_j}(\tau_i - \tau_j + 0^-) & g_{d_i a_j}(\tau_i - \tau_j + 0^-) \\ g_{b_i c_j}(\tau_i - \tau_j + 0^-) & g_{d_i c_j}(\tau_i - \tau_j + 0^-) \end{bmatrix}. \quad (14)$$

Eqs. (8) and (10) serve as the basis of interaction expansion continuous-time quantum Monte Carlo (CT-QMC): one generates random configurations $(v_1 \dots v_k)$ and evaluates the corresponding weight by computing the determinant [36, 37, 41].

B. Free energy expansion

While the partition function expansion can be efficiently computed as determinants (with scaling $\mathcal{O}(k^3)$) and the series is guaranteed to converge, it is also plagued by the negative sign problem, which is expected to worsen exponentially as the system size is increased or the temperature reduced. The sign problem is typically manageable in Hubbard model calculations up to moderate correlations and system size, where it only stems from negative determinant contributions. In contrast, the sign problem is particularly severe in molecules and surface science quantum impurity problems [41], where both Coulomb interaction terms and determinants generate negative coefficients.

In order to overcome these difficulties, we move to the grand potential Ω , defined as

$$Z_\xi = \exp(-\beta\Omega_\xi). \quad (15)$$

Ω_ξ serves as a cumulant-generating function for correlations functions [61] and its power series in ξ is given by:

$$\Omega_\xi = \Omega_0 - \frac{1}{\beta} \sum_{k=1}^{\infty} \xi^k \int d^k \mathcal{V} D_c(\mathcal{V}), \quad (16)$$

where Ω_0 is defined as $Z_0 = \exp(-\beta\Omega_0)$.

The symbol D_c indicates that unlike in Eq. (8), the sum is to be performed over connected Feynman diagrams only. Using an recursion formula similar to the one introduced in Ref. 52, D_c can be defined recursively:

$$D_c(\mathcal{V}) = D(\mathcal{V}) - \sum_{\mathcal{S} \subsetneq \mathcal{V}} \frac{|\mathcal{S}|}{|\mathcal{V}|} D_c(\mathcal{S}) D(\mathcal{V} \setminus \mathcal{S}). \quad (17)$$

A derivation is given in Appendix D. Eqs. (17) and (10) allow the computation of connected diagrams as a hierarchy of determinants at a cost of $\mathcal{O}(3^k)$.

We note that even in simple cases, the convergence radius R of the series (16) is not infinite, with the value of R depending on h , U , and β . Whenever $R < 1$, an order-by-order summation of the series will fail. We will discuss strategies to extend the convergence radius in Sec. II E.

For convergent series ($R > 1$), one can employ the diagrammatic Monte Carlo algorithm to sample the series (16) by generating random vertices and computing the weight using the recursion (17). One observes that the relative statistical error diverges exponentially with diagrammatic order k [62], which requires truncation of the series to a finite order k_{\max} .

C. Scattering amplitude expansion

Other than free energy, we are primarily interested in thermal correlation function of some operators $(\hat{X}_1, \dots, \hat{X}_m)$:

$$\langle \hat{X}_1 \dots \hat{X}_m \rangle := \frac{1}{Z} \text{Tr}[e^{-\beta(\hat{H} - \mu\hat{N})} \mathcal{T}(\hat{X}_1 \dots \hat{X}_m)], \quad (18)$$

in particular the single-particle Green's function:

$$G_{ba}(\tau) = -\langle \hat{c}_b(\tau) \hat{c}_a^\dagger(0) \rangle. \quad (19)$$

One can write down a diagrammatic expansion for the Green's function similar to Eq. (16) and a corresponding recursion relation [52]. We instead choose to perform the expansion for a vertex-like object.

In the case of the expansion of the free energy, the corresponding one-particle vertex is the scattering amplitude M [37, 38], defined as:

$$G(\tau) = g(\tau) + \int_0^\beta d\tau_1 d\tau_2 g(\tau - \tau_1) M(\tau_1 - \tau_2) g(\tau_2), \quad (20)$$

where multiplication is to be understood as matrix-matrix multiplication in spin-orbitals. Sampling a one-particle vertex is advantageous because it is independent of the choice of 'external legs' and thus allows measurements of both imaginary time-dependent quantities (G and Σ) and fixed-time quantities (density, kinetic energy, etc.) in the same simulation.

M arises naturally as a functional derivative of the grand potential:

$$M_{ab}(\tau) = \frac{\delta(\Omega - \Omega_0)}{\delta g_{ba}(-\tau)}. \quad (21)$$

We show this relation in Appendix B. Eq. (21) expresses the fact that by removing one line from a (closed) free-energy diagram, we get an interaction correction to the Green's function, which is exactly what the scattering amplitude encodes.

Combining Eq. (21) with Eq. (16) yields a series expansion for M :

$$M_{\xi,ab}(\tau) = -\frac{1}{\beta} \sum_{k=1}^{\infty} \xi^k \int d^k \mathcal{V} \frac{\delta D_c(\mathcal{V})}{\delta g_{ba}(-\tau)}. \quad (22)$$

We thus need to evaluate the functional derivative of the recursion relation (17).

We start with the derivative of the sum of all diagrams $D(\mathcal{V})$, where we rely on the following identity:

$$\frac{\delta \det A}{\delta A_{\alpha\beta}} = (\text{adj } A)_{\beta\alpha} := (-1)^{\alpha+\beta} \det A_{\bar{\alpha}\bar{\beta}}, \quad (23)$$

where A is an $n \times n$ matrix, $\text{adj}(A)$ denotes the $n \times n$ adjugate matrix of A , and $A_{\bar{\alpha}\bar{\beta}}$ is the $(n-1) \times (n-1)$ submatrix of A with the α -th row and β -th column removed. The adjugate matrix $\text{adj } A$ can be computed in $\mathcal{O}(n^3)$ time. The adjugate (or cofactor) matrix arises naturally in determinantal methods as a result of the Wick's theorem [37, 38, 63], and is often absorbed into the inverse matrix if the matrix A is not singular. In the context of CDet, however, care must be taken because A may be singular while $\text{adj } A$ is still meaningful [64]. We elaborate on the numerical calculation in Appendix E.

Combining Eq. (10) with Eq. (23), we have

$$\begin{aligned} \frac{\delta D(\mathcal{V})}{\delta g_{ba}(-\tau)} &= \prod_{i=1}^k \left(-\frac{U_{a_i b_i c_i d_i}}{4} \right) \\ &\times \sum_{\alpha, \beta}^{2n} [\text{adj } \mathbf{G}(\mathcal{V})]_{\alpha\beta} \delta_{a_\alpha a} \delta_{b_\alpha b} \\ &\times [\delta(\tau_\alpha - \tau_\beta - \tau) - \delta(\tau_\alpha - \tau_\beta + \beta - \tau)] \\ &= - \sum_{\alpha, \beta}^{2n} [\mathbf{A}(\mathcal{V})]_{\alpha\beta} \delta_{a_\alpha a} \delta_{b_\alpha b} \\ &\times [\delta(\tau_\alpha - \tau_\beta - \tau) - \delta(\tau_\alpha - \tau_\beta + \beta - \tau)] \end{aligned} \quad (24)$$

for $0 < \tau \leq \beta$, where a_α , b_β , and $\tau_{\alpha(\beta)}$ takes the same meaning as in Eq. (12), and we have defined the $2k \times 2k$ matrix

$$\mathbf{A}(\mathcal{V}) := - \prod_{i=1}^k \left(-\frac{U_{a_i b_i c_i d_i}}{4} \right) \text{adj } \mathbf{G}(\mathcal{V}), \quad (25)$$

which includes all connected and disconnected amputated diagrams in which internal legs corresponding to $\hat{c}_{a_\alpha}^\dagger(\tau_\alpha)$ and $c_{b_\beta}(\tau_\beta)$ are removed.

For the functional derivative of a *connected* free-energy diagram (26), the sum over all diagrams in Eq. (24) with amputated legs $\mathbf{A}(\mathcal{V})$ needs to be replaced with the sum over connected diagrams with amputated legs $\mathbf{A}_c(\mathcal{V})$:

$$\begin{aligned} \frac{\delta D_c(\mathcal{V})}{\delta g_{ba}(-\tau)} &= - \sum_{\alpha, \beta}^{2n} \{ [\mathbf{A}_c(\mathcal{V})]_{\alpha\beta} \delta_{a_\alpha a} \delta_{b_\alpha b} \\ &\times [\delta(\tau_\alpha - \tau_\beta - \tau) - \delta(\tau_\alpha - \tau_\beta + \beta - \tau)] \} \end{aligned} \quad (26)$$

for $0 < \tau \leq \beta$. The expansion of M (22) can now be expressed in terms of \mathbf{A}_c as

$$\begin{aligned} [M_\xi(\tau)]_{\alpha\beta} &= \frac{1}{\beta} \sum_{k=1}^{\infty} \xi^k \int d^k \mathcal{V} \sum_{\alpha, \beta}^{2n} \{ [\mathbf{A}_c(\mathcal{V})]_{\alpha\beta} \delta_{a_\alpha a} \delta_{b_\alpha b} \\ &\times [\delta(\tau_\alpha - \tau_\beta - \tau) - \delta(\tau_\alpha - \tau_\beta + \beta - \tau)] \}. \end{aligned} \quad (27)$$

The sum over connected amputated diagrams $\mathbf{A}_c(\mathcal{V})$ can be built up from an recursion technique similar to Eq. (17). Defining v_α and v_β as vertices where the α -th and β -th operators are located, respectively, diagrams in $[\mathbf{A}(\mathcal{V})]_{\alpha\beta}$ can always be partitioned to a connected part which contains v_α and v_β , and the disconnected vacuum diagrams, i.e.

$$[\mathbf{A}(\mathcal{V})]_{\alpha\beta} = \sum_{\substack{\mathcal{S} \subseteq \mathcal{V} \\ v_\alpha, v_\beta \in \mathcal{S}}} [\mathbf{A}_c(\mathcal{S})]_{\alpha'\beta'} D(\mathcal{V} \setminus \mathcal{S}), \quad (28)$$

where α', β' are row and column indices within \mathcal{S} that correspond to the row and column indices α, β in \mathcal{V} . Extracting the term with $\mathcal{S} = \mathcal{V}$, we have the recursion

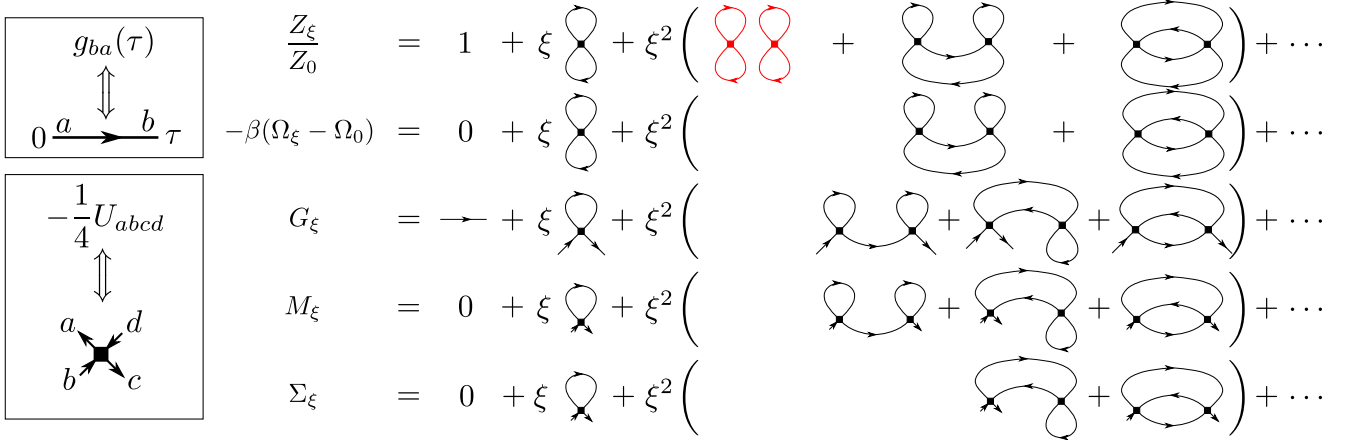


FIG. 1. Schematic example of diagrams up to order 2. Diagrams shown here should be understood as ‘labeled’ diagrams as described in Ref. [61]. Duplicate diagrams with the same topology are not shown. In the expansion of Z_ξ , the red diagram is an example of disconnected diagram, which is absent in the expansion of Ω due to linked cluster theorem.

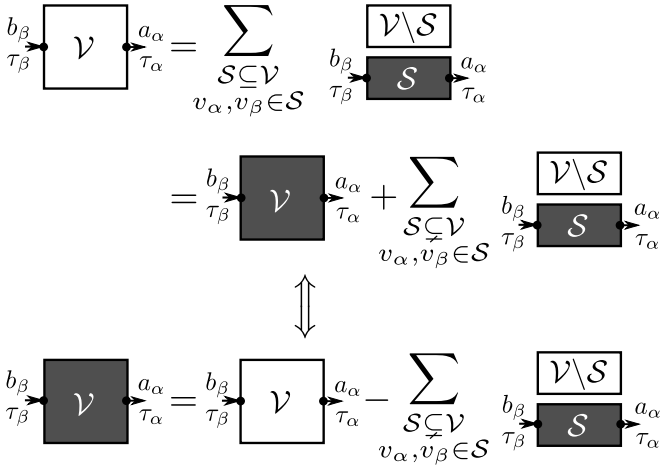


FIG. 2. Schematic illustration of the recursive removal of disconnected amputated diagrams. Empty boxes stand for the contribution of all diagrams (D or \mathbf{A}), and filled ones for that connected diagrams only (\mathbf{A}_c). Symbols inside boxes denote the set of vertices included in each component. The top relation shows all partitions of $[\mathbf{A}(\mathcal{V})]_{\alpha\beta}$ into a subset fully connected to the amputated legs and a disconnected complement set. It is reorganized as the bottom relation which recursively defines $\mathbf{A}_c(\mathcal{V})$ by removing all disconnected components.

relation for \mathbf{A}_c :

$$[\mathbf{A}_c(\mathcal{V})]_{\alpha\beta} = [\mathbf{A}(\mathcal{V})]_{\alpha\beta} - \sum_{\substack{\mathcal{S} \subsetneq \mathcal{V} \\ v_\alpha, v_\beta \in \mathcal{S}}} [\mathbf{A}_c(\mathcal{S})]_{\alpha'\beta'} D(\mathcal{V} \setminus \mathcal{S}). \quad (29)$$

This partitioning process is illustrated in Fig. 2. Since M captures the interaction correction to the Green’s function which starts at the first order in interaction, the zeroth order contribution $\mathbf{A}_c(\emptyset) = 0$. For each fixed \mathcal{V} , we apply Eq. (29) to recursively to compute $\mathbf{A}_c(\mathcal{V})$, which in turn yields M following Eq. (26). Algorithmically,

Eq. (29) can be evaluated by following Algorithm 1. Algorithm 1 runs in $\mathcal{O}(3^k k^2)$ time.

Algorithm 1 Recursive evaluation of $\mathbf{A}_c(\mathcal{V})$

Require: Vertices \mathcal{V} , $\mathbf{G}(\mathcal{V})$ defined in Eq. (13).

```

1: function RECURSION( $\mathcal{V}$ ,  $\mathbf{G}$ )
2:   if  $\mathcal{V} = \emptyset$  then
3:     return  $\mathbf{A}_c(\emptyset) = 0$ .
4:   else
5:     Compute  $\mathbf{A}(\mathcal{V})$  from  $\mathbf{G}$  following Eq. (25).
6:     Initialize  $\mathbf{A}_c(\mathcal{V}) \leftarrow \mathbf{A}(\mathcal{V})$ .
7:     for  $\mathcal{S} \subsetneq \mathcal{V}$  do
8:       Compute  $D(\mathcal{V} \setminus \mathcal{S})$  following Eq. (10).
9:        $\mathbf{A}_c(\mathcal{S}) \leftarrow \text{RECURSION}(\mathcal{S}, \mathbf{G}_{[\mathcal{S}, \mathcal{S}]})$ .  $\triangleright \mathbf{G}_{[\mathcal{S}, \mathcal{S}]}$ 
        is the submatrix of  $\mathbf{G}$  whose rows and columns correspond to
        the subset  $\mathcal{S}$ . Same definition applies to  $[\mathbf{A}_c(\mathcal{V})]_{[\mathcal{S}, \mathcal{S}]}$ .
10:      Subtract  $\mathbf{A}_c(\mathcal{S})D(\mathcal{V} \setminus \mathcal{S})$  from  $[\mathbf{A}_c(\mathcal{V})]_{[\mathcal{S}, \mathcal{S}]}$ .
11:    end for
12:    return  $\mathbf{A}_c(\mathcal{V})$ .
13:  end if
14: end function

```

D. Observables from scattering amplitude

The electron self-energy Σ relates the Green’s function G to the non-interacting propagator g via the Dyson’s equation

$$G(\tau) = g(\tau) + \int_0^\beta d\tau_1 d\tau_2 g(\tau - \tau_1) \Sigma(\tau_1 - \tau_2) G(\tau_2). \quad (30)$$

The expansion of the self-energy Σ can be interpreted as ‘one-particle irreducible’ (1-PI) amputated diagrams, which stay connected even when any single propagator line is removed (cf. Fig. 1). The self-energy is thus not directly sampled, M and Σ are related to each other by

[38]

$$\int_0^\beta d\tau' \Sigma(\tau - \tau') G(\tau') = \int_0^\beta d\tau' M(\tau - \tau') g(\tau') \quad (31)$$

Replacing G with Eq. (20), we have

$$\Sigma^{-1}(i\nu) = M(i\nu)^{-1} + g(i\nu), \quad (32)$$

where $X(i\nu)$ denotes the Fourier transform of $X(\tau)$ ($X = \Sigma, M, \dots$) and $i\nu$ is a fermionic Matsubara frequency.

The one- and two-body contribution to the electronic energy follow from Eqs. (30) and (20):

$$E = E_0 + E_V \quad (33a)$$

$$E_0 = \langle \hat{H}_0 \rangle = \frac{1}{\beta} \text{Tr}[hG] = \sum_{ab} h_{ab} \rho_{ab} \quad (33b)$$

$$\begin{aligned} E_V = \langle \hat{H}_V \rangle &= \frac{1}{2\beta} \text{Tr}[\Sigma G] \\ &= \frac{1}{2} \int_0^\beta d\tau \sum_{ab} M_{ab}(\tau) g_{ba}(-\tau). \end{aligned} \quad (33c)$$

Here $\rho_{ij} \equiv \langle \hat{c}_i^\dagger \hat{c}_j \rangle$ is the electron density matrix. Note that \hat{H}_0 does not include the Hartree and Fock terms of the interaction. See also Appendix C.

E. Hartree-Fock shifted Hamiltonian

In systems with significant electron-electron correlations where E_V has significant contribution to the full energy E , the perturbation expansions in Eqs. (16) and (22) may not converge at $\xi = 1$.

In order to achieve better convergence by starting from a ‘better’ non-interacting solution such that \hat{H}_0 is closer to \hat{H} , we change the partition of the Hamiltonian $\hat{H} = \hat{H}_0 + \hat{H}_V$ by adding physically-motivated counterterms to \hat{H}_0 and subtracting the same terms from \hat{H}_V . Such an approach is referred to the ‘ α -shift’ [37] or as the ‘shifted-action’ [65] in the action formalism.

We start by adding the simplest counterterm in the quadratic form

$$\Delta \hat{H}_\alpha = \sum_{ab} \alpha_{ab} \hat{c}_a^\dagger \hat{c}_b \quad (34)$$

to \hat{H}_0 and subtract it from \hat{H}_V , such that

$$\hat{H}_{0,\alpha} = \sum_{ab} (h_{ab} + \alpha_{ab}) \hat{c}_a^\dagger \hat{c}_b \quad (35)$$

$$\hat{H}_{V,\alpha} = \frac{1}{4} \sum_{abcd} U_{abcd} \hat{c}_a^\dagger \hat{c}_c^\dagger \hat{c}_d \hat{c}_b - \alpha_{ab} \hat{c}_a^\dagger \hat{c}_b. \quad (36)$$

The total Hamiltonian $\hat{H} = \hat{H}_{0,\alpha} + \hat{H}_{V,\alpha}$ is unchanged, whereas the perturbation expansion of $\hat{H}_\xi = \hat{H}_{0,\alpha} + \xi \hat{H}_{V,\alpha}$ can be controlled by choosing different α . The

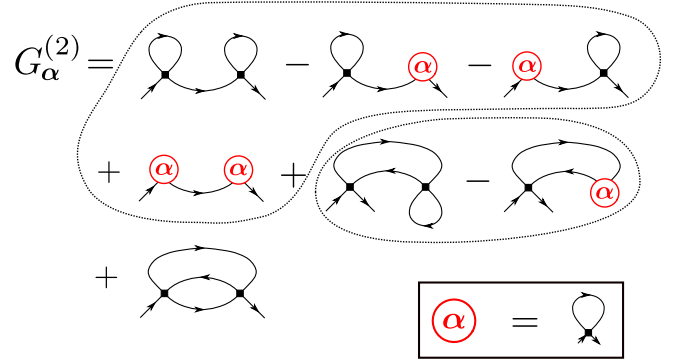


FIG. 3. Schematic example of diagram cancellations due to the Hartree-Fock counterterm. Here we show all second-order Green’s function diagrams generated by the counterterm, where the red circle indicates the counterterm α , each introduces a factor of -1 . Terms in each dashed curve cancel each other, leaving only the last term.

counterterm need not be quadratic in general. Though quadratic choices are convenient in the determinantal setup, recursion schemes have been developed for general counterterms [55].

The shifted non-interacting propagator

$$g^\alpha(\tau) = [(-\partial_\tau + \mu)\mathbf{1} - h - \alpha]_{aa'}^{-1} \quad (37)$$

can be seen as a Green’s function with an *a priori* self-energy α .

In the molecular context, a significant contribution to electron correlations can be obtained by the Hartree-Fock approximation. We therefore choose α to be the Hartree-Fock self-energy, i.e. Σ_{HF} . Σ_{HF} is given by the self-consistent equations at finite temperature

$$[\Sigma_{\text{HF}}]_{ab} = \sum_{cd} U_{abcd} \rho_{cd}, \quad (38a)$$

$$\rho = f(h + \Sigma_{\text{HF}} - \mu\mathbf{1}). \quad (38b)$$

Here $f(A) = [\mathbf{1} + \exp(\beta A)]^{-1}$ is the matrix-valued Fermi distribution function, and μ is the chemical potential which may be adjusted so that the total number of electrons in the system is adjusted to charge neutrality.

Diagrammatically, the Hartree-Fock shift renormalizes the propagators lines to g_α , and an additional effective two-point vertex α has to be included in diagrams. The effective vertex α cancels any diagram which has at least one vertex connecting to itself with *exactly* one propagator line. This removes all ‘tadpole’ diagrams in expansions of G and M , as well as that of Ω except for the first order diagram whose vertex connects to itself with two propagator lines. Fig. 3 illustrates the cancellation of such diagrams.

Given a specific set of vertices \mathcal{V} , the removal of all tadpole diagrams is achieved by replacing the \mathbf{G} matrix

(13) defined on internal vertices \mathcal{V} with:

$$\mathbf{G}(\mathcal{V}) := \begin{bmatrix} \mathbf{0} & g_{12}^\alpha & \cdots & g_{1n}^\alpha \\ g_{21}^\alpha & \mathbf{0} & \cdots & g_{2n}^\alpha \\ \vdots & \vdots & \ddots & \vdots \\ g_{n1}^\alpha & g_{n2}^\alpha & \cdots & \mathbf{0} \end{bmatrix} \quad (39)$$

$$g_{ij}^\alpha := \begin{bmatrix} g_{b_i a_j}^\alpha(\tau_i - \tau_j + 0^-) & g_{d_i a_j}^\alpha(\tau_i - \tau_j + 0^-) \\ g_{b_i c_j}^\alpha(\tau_i - \tau_j + 0^-) & g_{d_i c_j}^\alpha(\tau_i - \tau_j + 0^-) \end{bmatrix}.$$

i.e. by setting all 2×2 diagonal blocks (corresponding to self-connections of vertices) to zero, and replacing bare propagators with g^α . Using the modified definition of \mathbf{G} in Eqs. (10) and (25), one can carry out the same recursive calculations in Eq. (26) to obtain corresponding connected quantities.

Note that this introduces a bias in the free-energy evaluation by setting the first order contribution (the ‘dumb-bell’ diagram) to zero, which needs to be corrected:

$$\begin{aligned} \Omega_\alpha^{(1)} &= \frac{1}{2} \sum_{abcd} U_{abcd} g_{ba}^\alpha(0^-) g_{dc}^\alpha(0^+) - \sum_{ab} \alpha_{ab} g_{ba}^\alpha(0^-) \\ &= -\frac{1}{2} \sum_{ab} [\Sigma_{\text{HF}}]_{ab} [\rho_{\text{HF}}]_{ba}. \end{aligned} \quad (40)$$

In the remainder of this paper, we will always use a Hartree-Fock counterterm and omit the α subscripts.

F. Monte Carlo integration of diagrammatic series

Evaluations of diagrammatic series, such as Eqs. (16) and (27), can be formally summarized as

$$X = \sum_{k=0}^{\infty} \int d^k \mathcal{V} \mathcal{C}(\mathcal{V}), \quad (41)$$

where X is the physical variable (G , M , ...), $\mathcal{V} = (v_1, \dots, v_k)$ denotes space time indices of internal vertices, and \mathcal{C} the contribution of each fixed configuration of \mathcal{V} to X . Here we take the ‘physical’ value of the coupling constant $\xi = 1$. To perform a Monte Carlo integral, we introduce a cutoff k_{max} of the expansion order, and an *a priori* probability distribution of vertex space-time indices $p(\mathcal{V})$ such that

$$p(\mathcal{V}) \geq 0, \quad \sum_{k=0}^{k_{\text{max}}} \int d^k \mathcal{V} p(\mathcal{V}) \equiv 1. \quad (42)$$

In addition, we require that $p(\mathcal{V}) > 0$ whenever $\mathcal{C}(\mathcal{V}) \neq 0$. The order- k_{max} approximation to X can be estimated stochastically as

$$\begin{aligned} X_{k_{\text{max}}} &= \sum_{k=0}^{k_{\text{max}}} \int d^k \mathcal{V} \frac{\mathcal{C}(\mathcal{V})}{p(\mathcal{V})} p(\mathcal{V}) = \left\langle \frac{\mathcal{C}}{p} \right\rangle_p \\ &\approx \frac{1}{N} \sum_{i=1}^N \frac{\mathcal{C}(\mathcal{V}_i)}{p(\mathcal{V}_i)}, \quad \mathcal{V}_1, \dots, \mathcal{V}_N \sim p \end{aligned} \quad (43)$$

with a large number N of Monte Carlo samples $\{\mathcal{V}_i\}$ generated following distribution $p(\mathcal{V})$.

Since the Green’s function G , self-energy Σ , as well as the total electronic energy $E = E_0 + E_V$ can all be derived from the scattering matrix M using Eqs. (20), (32), (33), it is sufficient to only keep track of the amputated diagrams $\mathbf{A}_c(\mathcal{V})$ and obtain all other observables as derived quantities. Table I summarizes some of these measurements. In our implementation, we only measure the energy and $M(i\nu_n)$ with fermionic Matsubara frequencies $i\nu_n$ on the fly, and construct $G(i\nu_n)$ and $\Sigma(i\nu_n)$ from $M(i\nu_n)$ following

$$G(i\nu_n) = g(i\nu_n) + g(i\nu_n)M(i\nu_n)g(i\nu_n), \quad (44)$$

$$\Sigma(i\nu_n) - \Sigma_{\text{HF}} = [M(i\nu_n)^{-1} + g(i\nu_n)]^{-1} \quad (45)$$

for each frequency, where symbols with ‘hats’ represent quantities in frequency representation as matrices in spin-orbital indices. Resampling techniques such as the jack-knife or the bootstrap are applied to avoid biased error estimations.

For efficient Monte Carlo simulations, it is important to choose the *a priori* distribution $p(\mathcal{V})$ to achieve importance sampling, such that the simulation samples more frequently when $|\mathcal{C}(\mathcal{V})|$ is large and less frequently otherwise. Since we measure multiple observables in one simulation, we need to define such a distribution that works for all measurements. We find in practice that the following choices provides efficient samplings for most measurements:

$$p_{\mathbf{A}}(\mathcal{V}) = \frac{\|\mathbf{A}_c(\mathcal{V})\|}{W_{\mathbf{A}}}, \quad W_{\mathbf{A}} = \sum_{k=0}^{k_{\text{max}}} \int d^k \mathcal{V} \|\mathbf{A}_c(\mathcal{V})\|, \quad (46)$$

$$p_E(\mathcal{V}) = \frac{|\epsilon(\mathcal{V})|}{W_E}, \quad W_E = \sum_{k=0}^{k_{\text{max}}} \int d^k \mathcal{V} |\epsilon(\mathcal{V})|, \quad (47)$$

where $\|\cdot\|$ denotes the Frobenius norm of a matrix, and $\epsilon(\mathcal{V})$ is the energy measurement defined in Table I

$$\begin{aligned} \epsilon(\mathcal{V}) &= \frac{1}{2\beta} \sum_{\alpha\beta=1}^{2|\mathcal{V}|} [\mathbf{A}_c(\mathcal{V})]_{\alpha\beta} \left\{ g_{b_\beta a_\alpha}(\tau_\beta - \tau_\alpha) + \right. \\ &\quad \left. + \sum_{ab} [2h + \Sigma_{\text{HF}}]_{ab} [g_{ba_\alpha} * g_{b_\beta a}] (\tau_\beta - \tau_\alpha) \right\}, \end{aligned} \quad (48)$$

where $[f * g](\tau) = \int_0^\beta d\tau' f(\tau - \tau') g(\tau')$ denotes a convolution in τ . p_E performs well for the energy measurements, whereas $p_{\mathbf{A}}$ is more robust when measurement of M is needed.

At high expansion order k_{max} , the normalization factors $W_{\mathbf{A}}$ and W_E are difficult to calculate analytically. Instead, we measure an auxillary quantity whose exact value can be calculated analytically, and normalize all other measurements against it. For example, we can normalized against the second-order contribution to the total energy

$$E^{(2)} = \left\langle \frac{\epsilon(\mathcal{V}) \delta_{|\mathcal{V}|,2}}{p_E(\mathcal{V})} \right\rangle_{p_E} = W_E \langle \text{sgn}[\epsilon(\mathcal{V})] \delta_{|\mathcal{V}|,2} \rangle_{p_E}. \quad (49)$$

TABLE I. Measurements for physical observables. The imaginary time convolution is defined as $[f * g](\tau) = \int_0^\beta d\tau' f(\tau - \tau')g(\tau')$. E_0^{HF} and E_V^{HF} are kinetic and potential energies from the Hartree-Fock solution.

X	$\mathcal{C}(\mathcal{V})$
$M_{ab}(\tau)$	$\frac{1}{\beta} \sum_{\alpha, \beta=1}^{2 \mathcal{V} } [\mathbf{A}_c(\mathcal{V})]_{\alpha\beta} \delta_{a\alpha} \delta_{b\beta} [\delta(\tau_\alpha - \tau_\beta - \tau) - \delta(\tau_\alpha - \tau_\beta + \beta - \tau)]$
$M_{ab}(i\nu_n) = \int_0^\beta d\tau M_{ab}(\tau) e^{i\nu_n \tau}$	$\frac{1}{\beta} \sum_{\alpha, \beta=1}^{2 \mathcal{V} } [\mathbf{A}_c(\mathcal{V})]_{\alpha\beta} \delta_{a\alpha} \delta_{b\beta} e^{i\nu_n(\tau_\alpha - \tau_\beta)}$
$G_{ba}(i\nu_n) - g_{ba}(i\nu_n) = [gMg]_{ba}$	$\frac{1}{\beta} \sum_{\alpha, \beta=1}^{2 \mathcal{V} } [\mathbf{A}_c(\mathcal{V})]_{\alpha\beta} g_{ba\alpha}(i\nu_n) g_{b\beta a}(i\nu_n) e^{i\nu_n(\tau_\alpha - \tau_\beta)}$
$E_0 - E_0^{\text{HF}}$	$\frac{1}{\beta} \sum_{\alpha, \beta=1}^{2 \mathcal{V} } [\mathbf{A}_c(\mathcal{V})]_{\alpha\beta} \sum_{ab} h_{ab} [g_{ba\alpha} * g_{b\beta a}](\tau_\beta - \tau_\alpha)$
$E_V - E_V^{\text{HF}}$	$\frac{1}{2\beta} \sum_{\alpha, \beta=1}^{2 \mathcal{V} } [\mathbf{A}_c(\mathcal{V})]_{\alpha\beta} \left\{ g_{b\beta a\alpha}(\tau_\beta - \tau_\alpha) + \sum_{ab} [\Sigma_{\text{HF}}]_{ab} [g_{ba\alpha} * g_{b\beta a}](\tau_\beta - \tau_\alpha) \right\}$

Here we have chosen p_E as the *a priori* distribution. Any other measurements can now be estimated as

$$X = \left\langle \frac{\mathcal{C}(\mathcal{V})}{p_E(\mathcal{V})} \right\rangle_{p_E} = W_E \left\langle \frac{\mathcal{C}(\mathcal{V})}{\epsilon(\mathcal{V})} \right\rangle_{p_E} = E^{(2)} \frac{\langle \mathcal{C}(\mathcal{V}) / \epsilon(\mathcal{V}) \rangle_{p_E}}{\langle \text{sgn}[\epsilon(\mathcal{V})] \delta_{|\mathcal{V}|,2} \rangle_{p_E}}. \quad (50)$$

Similar relations apply when we use other choices of *a priori* distributions or normalization measurements.

Once $p(\mathcal{V})$ is defined, we generate Monte Carlo samples as a Markov chain via the Metropolis-Hastings algorithm. From each configuration \mathcal{V}_i , a new configuration \mathcal{V}_j is proposed following some *proposal probability* distribution $w^{\text{prop}}(\mathcal{V}_j|\mathcal{V}_i)$. To ensure detailed balance, an acceptance ratio R is calculated after each proposal as

$$R(\mathcal{V}_j|\mathcal{V}_i) = \frac{w^{\text{prop}}(\mathcal{V}_i|\mathcal{V}_j)p(\mathcal{V}_j)}{w^{\text{prop}}(\mathcal{V}_j|\mathcal{V}_i)p(\mathcal{V}_i)}. \quad (51)$$

The proposal $\mathcal{V}_i \rightarrow \mathcal{V}_j$ is accepted with probability

$$w^{\text{acc}}(\mathcal{V}_j|\mathcal{V}_i) = \min(1, R(\mathcal{V}_j|\mathcal{V}_i)). \quad (52)$$

This ensures the detailed balance of the Markov process, i.e.

$$w(\mathcal{V}_j|\mathcal{V}_i)p(\mathcal{V}_i) = w(\mathcal{V}_i|\mathcal{V}_j)p(\mathcal{V}_j), \quad (53)$$

where

$$w(\mathcal{V}_j|\mathcal{V}_i) = w^{\text{acc}}(\mathcal{V}_j|\mathcal{V}_i)w^{\text{prop}}(\mathcal{V}_j|\mathcal{V}_i)p(\mathcal{V}_i). \quad (54)$$

which guarantees samples obtain the equilibrium distribution $p(\mathcal{V})$ after thermalization.

In molecular systems, due to the complexity in the multi-orbital Coulomb interaction tensor, as well as the energy differences in non-interacting energy levels, the configuration space of the Monte Carlo can be uneven and may lead to ergodicity problems in the random walk.

We design the following set of updates which lead to an ergodic random walk in the configuration space for all systems we investigate in Sec. III.

1. **Vertex splitting:** Split a random vertex $v = (a, b, c, d; \tau)$ to two new vertices $v_1 = (a, b, c', d'; \tau)$ and $v_2 = (a', b', c, d; \tau')$. The new indices a', b', c', d' , and τ' can be proposed by some *a priori* probability p^{ins} . The proposal probability distribution for this update from order k to $k+1$ is

$$w^{\text{prop}}(v_1, v_2; k+1|v; k) = \frac{p^{\text{ins}}(a', b', c', d', \tau')}{k} \quad (55)$$

2. **Vertex merging:** Pick two random vertices $v_1 = (a, b, c', d'; \tau)$ and $v_2 = (a', b', c, d; \tau')$ and merge them into $v = (a, b, c, d; \tau)$. The proposal probability distribution from order $k+1$ to k is

$$w^{\text{prop}}(v; k|v_1, v_2; k+1) = \frac{1}{k(k+1)}. \quad (56)$$

3. **Vertex shift in time:** Update the time label τ of a vertex v to a new value τ' .

4. **Vertex shift in orbitals:** Update one of the orbital labels a, b, c, d of a vertex v to a random new value.

Vertex shift in time or orbitals are self-balancing moves, hence the acceptance ratios shares the same form

$$R(\mathcal{V}_2|\mathcal{V}_1) = \frac{p(\mathcal{V}_2)}{p(\mathcal{V}_1)}. \quad (57)$$

Vertex splitting and merging are mutually inverse updates. The acceptance ratios are therefore

$$\begin{aligned} R(v_1, v_2; k+1|v; k) &= R(v; k|v_1, v_2; k+1)^{-1} \\ &= \frac{w^{\text{prop}}(v; k|v_1, v_2; k+1)p(v_1, v_2; k+1)}{w^{\text{prop}}(v_1, v_2; k+1|v; k)p(v; k)} \\ &= \frac{k+1}{p^{\text{ins}}(a', b', c', d', \tau')} \frac{p(v_1, v_2; k+1)}{p(v; k)}. \end{aligned} \quad (58)$$

There is considerable freedom in choosing p^{ins} . For all systems we study in this work, we choose p^{ins} such that

$$p^{\text{ins}}(a', b', c', d', \tau') = p^{\text{orb}}(a', b', c', d') p^{\text{time}}(\tau'), \quad (59)$$

where $p^{\text{orb}}(a', b', c', d')$ is uniformly distributed if the inserted indices can form non-zero propagator connections and zero otherwise, and

$$p^{\text{time}}(\tau') = \varphi(|\tau' - \bar{\tau}_V|) \quad (60)$$

where $\bar{\tau}_V = \frac{1}{k} \sum_{i=1}^k \tau_k$ is the average time coordinate of the existing vertices, and we choose $\varphi(\tau)$ as a function in $[0, \beta]$ which has more weight near $\tau = 0$ and β but still non-negligible weight in between. Since the Hartree-Fock propagators decay exponentially away from 0 and β , this makes sure that the new vertex are more likely to stay close to existing vertices so that the resulting configuration has sizable contribution. In our implementation, we define

$$f(\tau) = \frac{\lambda}{\arctan(\beta\lambda)} \left\{ \frac{1}{1 + (\tau\lambda)^2} + \frac{1}{1 + [(\beta - \tau)\lambda]^2} \right\}, \quad (61)$$

as a Lorentzian distribution where λ is an estimation of the overall energy scale of the system proportional to e.g. the standard deviation of the Hartree-Fock energy levels.

III. RESULTS

A. Series convergence

We first present a test of our method on a minimal molecular system: H_2 in the STO-6g basis set [66]. Two hydrogen atoms are placed at distance r and finite temperature $T = 1/\beta$. The basis set only contains the 1s orbital in each atom. This setup allows us to easily perform exact diagonalization (ED) calculations of the full molecular Hamiltonian at any temperature, such that exact benchmark results for our CDet results are available.

In Fig. 4, we compare the total energy E_{tot} from CDet with order truncation k_{max} up to 6 to the ED energy at $T = 50^{-1} E_h$, both as a function of r . Around equilibrium distance $r \approx 1.4 a_0$, the CDet energy converges well to the ED solution. The system moves to the strongly correlated regime (i.e. a regime far from the Hartree-Fock solution), as we ‘stretch’ the molecule by increasing r . At $r > 2.0 a_0$ we start to observe significant systematic deviation at $k_{\text{max}} = 6$. Since the kinetic energy of electrons moving between two atoms is significantly reduced as we increase r but the long-range Coulomb repulsion between electrons changes slowly, the electron-electron interaction becomes more important at larger r , and hence it is expected that the perturbation expansion becomes more difficult to converge. This setup is standard in quantum chemistry [67] and is similar in spirit to lattice model setups in which a metal-to-insulator transition is induced by gradually increasing an on-site interaction.

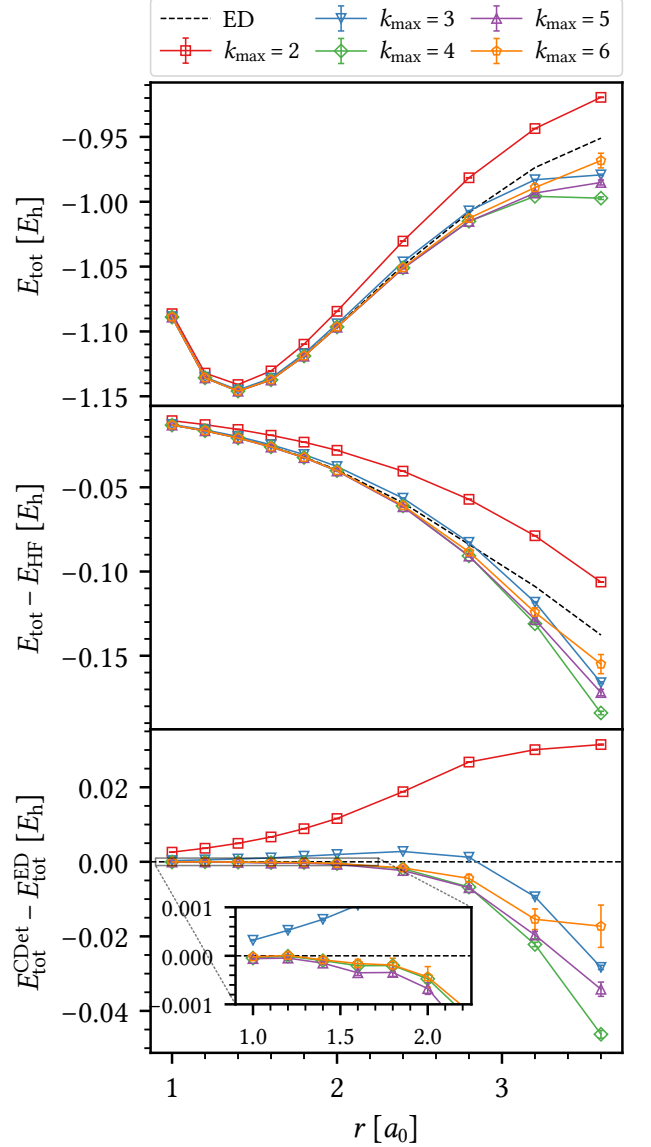


FIG. 4. Total energy E_{tot} with Monte Carlo errors for H_2 , STO-6g, $T = 50^{-1} E_h$. Top panel: comparison of ED and CDet at different k_{max} . Middle panel: total energy with Hartree-Fock contribution removed. Bottom panel: difference between ED and CDet.

Analytically, the convergence behavior is determined by the properties of the expanded quantity (e.g. $E[\xi]$) as a function of the coupling constant ξ on the complex plane, similar to the convergence analysis for many-body perturbation theory (MBPT) calculations at $T = 0$ [68–72]. We evaluate the electron energy $E[\xi]$ for complex values of ξ near $\xi = 0$ using ED at $r = 1.4, 2.0, 2.8$, and

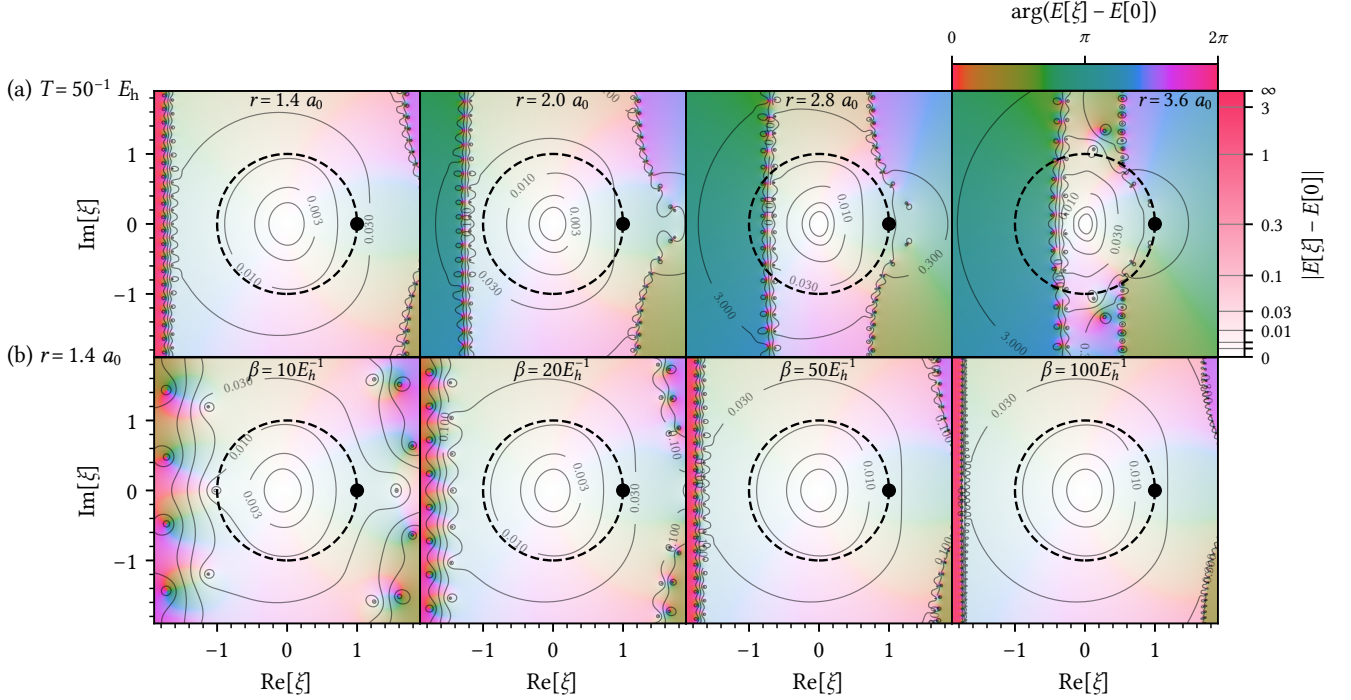


FIG. 5. Analytic structure of electron total energy evaluated with ED as a function of the complex coupling constant ξ . H_2 , STO-6g. Colors represent complex phases and brightness indicates the magnitude (see color bars). The black dot at $\xi = 1$ represents the ‘physical’ result. The dashed black circle indicates minimum convergence radius necessary for the perturbation series to converge at $\xi = 1$. (a) Effect of changing r at fixed temperature $T = 50^{-1} E_h$. At $r = 1.4 a_0$ and $r = 2.0 a_0$, no singularity is visible in the unit circle and the series is convergent at $\xi = 1$. At $r = 2.8 a_0$ and $3.6 a_0$, poles appear in the unit circle, resulting in a divergent series at $\xi = 1$. (b) Effect of changing T at fixed $r = 1.4 a_0$. The real-axis locations of the vertical ‘walls’ of poles does not change significantly as temperature decreases, while the imaginary-axis spacing of the poles decreases proportionally with T .

$3.6 a_0$, following

$$Z[\xi] = \text{Tr} \left\{ e^{-\beta[(\hat{H}_0 + \hat{H}_\alpha) + \xi(\hat{H}_V - \hat{H}_\alpha) - \mu\hat{N}]} \right\}, \quad (62)$$

$$E[\xi] = \frac{1}{Z[\xi]} \text{Tr} \left\{ [(\hat{H}_0 + \hat{H}_\alpha/2) + \xi(\hat{H}_V - \hat{H}_\alpha/2)] \right. \\ \left. \times e^{-\beta[(\hat{H}_0 + \hat{H}_\alpha) + \xi(\hat{H}_V - \hat{H}_\alpha) - \mu\hat{N}]} \right\}, \quad (63)$$

where \hat{H}_α is the Hartree-Fock counterterm introduced in Sec. II E. One can show via a straight forward substitution that $E[1]$ gives the ‘physical’ electron energy and $E[0]$ recovers the Hartree-Fock energy. Figure 5.a shows the interaction correction $E[\xi] - E[0]$ to the total energy, where the black dot represents the physical value at $\xi = 1$. Since the convergence radius of the power series around $\xi = 0$ is determined by the singularity (pole or branch cut) closest to the origin, the series is convergent at the ‘physical’ point $\xi = 1$ if and only if there are no singularities in the unit circle (dashed circles in Fig. 5). At $r = 1.4 a_0$, all poles are far outside the unit circle, indicating a rapidly convergent series. As we increase r , poles move closer to the unit circle at $r = 2.0 a_0$, implying a slower convergence of the series, and finally enter the unit circle at $r = 2.8 a_0$ and $3.6 a_0$, resulting in divergent series at $\xi = 1$.

The analytic properties are reflected directly in the convergence behavior of the CDet results. For a direct comparison, we calculate the contribution of each order k to the total energy $E_{\text{tot}}^{(k)}$ up to $k_{\text{max}} = 8$ for the same values of r , as shown in Fig. 6. At $r = 1.4 a_0$, $E_{\text{tot}}^{(k)}$ quickly converges to zero at $k > 4$. At $r = 2.0 a_0$, we observe tendency to converge at $k = 8$ but non-zero systematic deviations remain. For $r = 2.8 a_0$ and $3.6 a_0$, no signs of convergence are observed up to $k = 8$.

The CDet approach can be applied to different temperatures without adding significant computational cost, as we will show in Sec. III B. This is fundamentally different from methods such as CT-QMC, where reaching lower T is only possible at an exponential cost away from half filling [36]. In Fig. 7, we show the temperature dependence of the CDet total energy for H_2 , STO-6g at $k_{\text{max}} = 6$, from $T = 10.0^{-1} E_h$ down to $T = 500.0^{-1} E_h$, in comparison to the ED solution at $T = 0$. All calculations use the same algorithmic setup and the same number of Monte Carlo steps. Convergence to the zero-temperature solution is observed as T decreases, while the stochastic error estimation does not change significantly. Systematic deviations can be observed at similar locations ($r > 2.0 a_0$) for different temperatures, indicat-

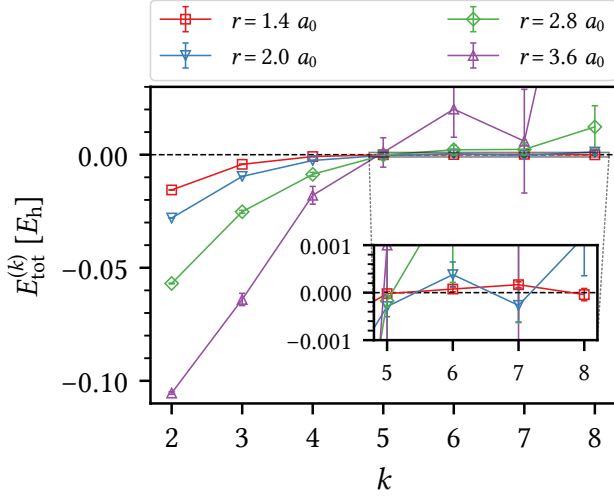


FIG. 6. Contribution $E_{\text{tot}}^{(k)}$ of each order k to total energy. H_2 , STO-6g, $T = 50^{-1} E_h$. Convergence is observed at bond lengths $r \leq 2.0 a_0$ but not at $r \geq 2.8 a_0$.

ing similar convergence behavior for the same system at different temperature. This can be shown by the temperature dependence of the analytic structure of $E[\xi]$, as plotted in Fig. 5.b. As temperature is reduced, the spacing of the poles along the imaginary direction decreases proportionally, but the real-axis locations of the vertical ‘walls’ of poles stay almost unchanged, which leads to similar convergence radii at different temperature.

The Hartree-Fock shifted action plays an important role in achieving better series convergence in CDet. Figure 8 compares the ED analytic structure of the total energy $E[\xi]$ with and without the Hartree-Fock shift. Without the shift, even for the equilibrium distance $r = 1.4 a_0$ (usually considered ‘weakly correlated’), there are poles deep inside the unit circle, implying a highly divergent series at $\xi = 1$. In contrast, the Hartree-Fock shift pushes the poles away from the origin, which leads to a convergent series as seen in Fig. 4 and Fig. 6.

The CDet approach gives access to dynamic quantities, such as the Green’s function G and the self-energy Σ , through the scattering amplitude M . The left column of Fig. 9 shows the CDet measurement of $\hat{M}(i\omega_n)$ in Matsubara frequency space up to $k_{\text{max}} = 6$ for H_2 , STO-6g at $r = 1.4 a_0$ and $T = 50^{-1} E_h$. As we increase the expansion order, CDet results gradually converge to the ED solution (black lines), and at order 6 we observe only a small systematic error due to order truncation. The CDet self-energy Σ is calculated from M following Eq. (45). Both quantities exhibit similar behavior, as shown in the right column of Fig. 9. At order 3 and higher, the real part of $\hat{\Sigma}(i\omega_n)$ takes non-zero value at high-frequency limit, corresponding to the correction to the frequency-independent Hartree-Fock self-energy Σ_{HF} . The CDet Green’s function, derived from M following Eq. (44), is shown in Fig. 10. Good agreement

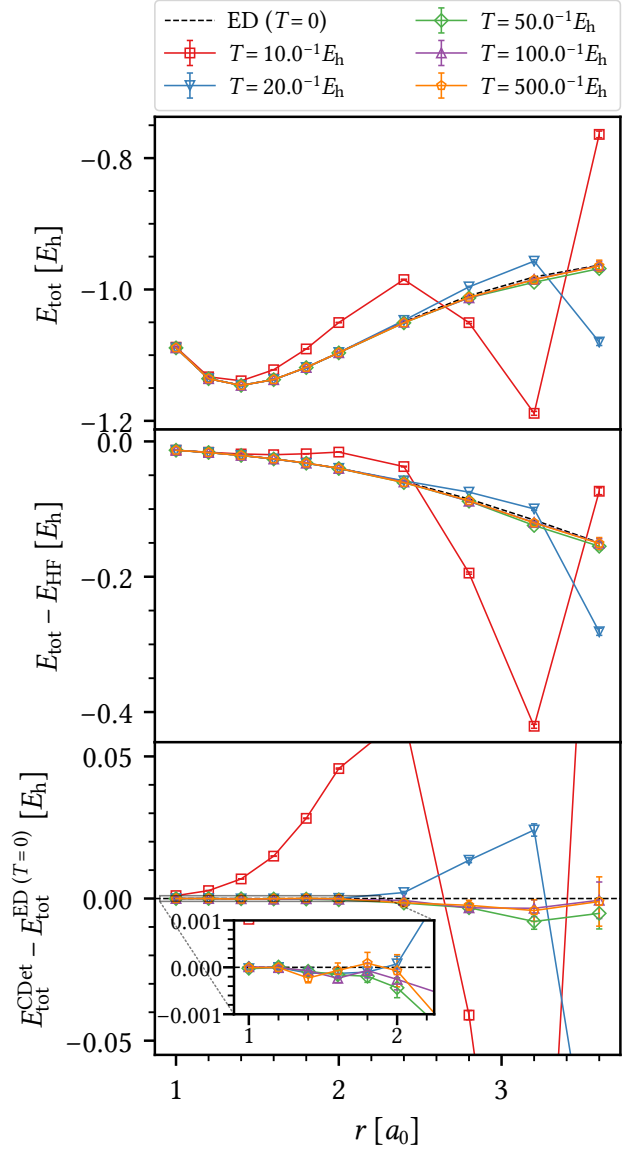


FIG. 7. Temperature dependence of CDet total energy E_{tot} for H_2 , STO-6g, $k_{\text{max}} = 6$. Top panel: comparison of ED at $T = 0$ and CDet at different T . Middle panel: total energy with Hartree-Fock contribution removed. Bottom panel: difference between ED and CDet.

with ED is observed at $k_{\text{max}} = 6$ on the top panel, where both the Monte Carlo error estimation and the systematic error due to order truncation is much smaller than the symbol size. The bottom panel shows convergence of CDet Green’s function to ED by increasing k_{max} , with a small but visible systematic deviation at low frequency when $k_{\text{max}} = 6$.

The generality of our CDet implementation allows a straightforward extension to much larger basis sets. Going beyond the minimal basis, we compute the CDet total energy of H_2 using cc-pVDZ and cc-pVTZ basis sets with 10 and 28 orbitals in total, respectively, and compare to

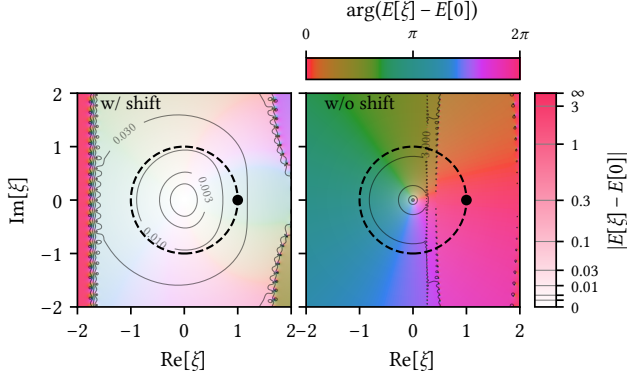


FIG. 8. Analytic structure of electron total energy as a function of a complex coupling constant ξ with and without Hartree-Fock shift. Left (right) panel presents values of $E[\xi] - E[0]$ evaluated on the complex plane for H_2 , STO-6g, $T = 50^{-1} E_h$ and $r = 1.4 a_0$ with (without) Hartree-Fock shift.

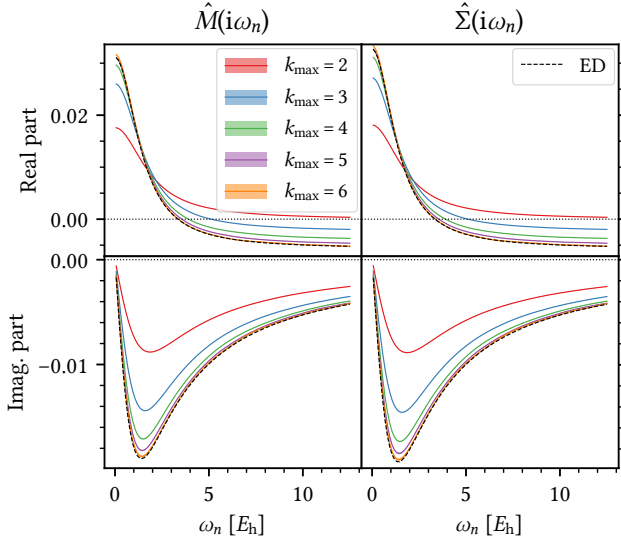


FIG. 9. CDet dynamic quantities for H_2 , STO-6g, $T = 50^{-1} E_h$, $r = 1.4 a_0$. Shadings indicate Monte Carlo error estimates. Left column: Measured CDet $\text{Re}M(i\omega_n)$ (top panel) and $\text{Im}M(i\omega_n)$ (bottom panel) compared to ED. Right column: CDet self-energy in comparison to ED (excluding Hartree-Fock contribution Σ_{HF}), top (bottom) panel showing real (imaginary) part of $\Sigma(i\omega_n)$. Here we show the diagonal matrix element at orbital 1 for both M and Σ .

the ED solution as shown in Fig. 11. For $r < 2.0 a_0$, CDet gives decent convergence to ED at $k_{\text{max}} = 4$, with both stochastic and systematic error below $1 mE_h$. The 2s and 2p orbitals added by cc-pVDZ basis and 3s, 3p and 3d orbitals by cc-pVTZ basis are mostly unoccupied, and the most electron excitation occur near the lowest 1s orbitals. Consequently, the convergence behavior and computational cost of CDet do not change significantly

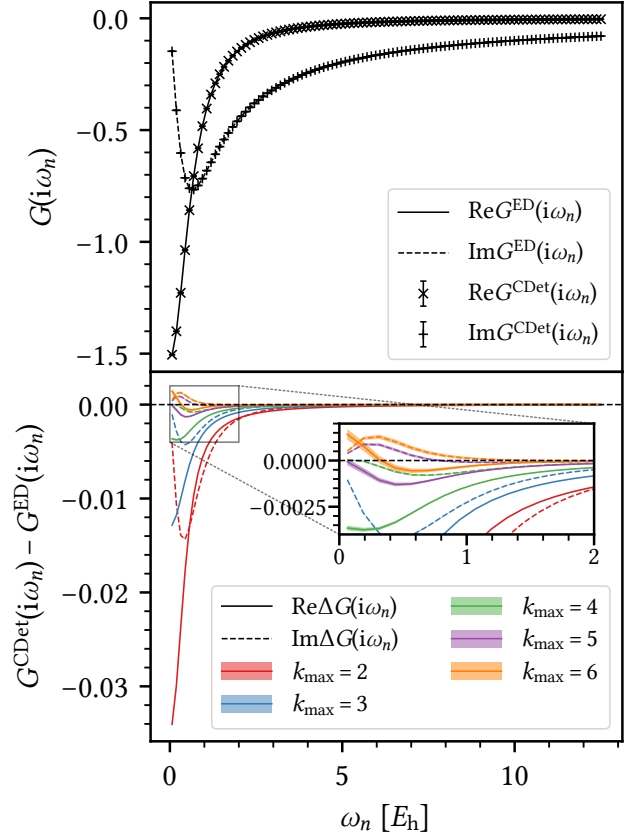


FIG. 10. CDet Green's function in comparison to ED. H_2 , STO-6g, $T = 50^{-1} E_h$, $r = 1.4 a_0$ Top panel: values of $\hat{G}(i\omega_n)$ at orbital 1. CDet results at $k_{\text{max}} = 6$ are plotted as symbols and ED values as lines. Error bars are indicated but much smaller than symbol size. Bottom panel: deviations of CDet results from ED at different k_{max} . Solid (dashed) lines represent real (imaginary) part of $\hat{G}_{11}(i\omega_n)$. Shadings indicate stochastic uncertainties of CDet.

from the minimal basis STO-6g.

Finally, we extend our method to bigger molecules by adding more hydrogen atoms to the system. We consider a chain of 10 hydrogen atoms on a straight line with equal spacing r , the same benchmark system used in Ref. 59. At minimal basis STO-6g, all ten 1s orbitals contribute equally to the active space of 10 electrons. Compared to H_2 with cc-pVDZ, which has the same number of orbitals, H_{10} with STO-6g has more orbitals relevant to electron correlations, and the cost of CDet is higher (for a detailed analysis see Sec. III B). The left column of Fig. 12 plots the CDet total energy up to $k_{\text{max}} = 4$ in comparison to ED solution at $T = 50^{-1} E_h$. Convergence within $5 mE_h$ is achieved at $k_{\text{max}} = 4$ for $r < 2.4 a_0$, and systematic deviations are evident for $r > 2.4 a_0$. Similar behavior can be found in the the zero-temperature coupled cluster (CCSD) result (dotted lines), as both methods rely on the perturbative expansions of electron-electron interactions in different forms. The computational cost becomes much

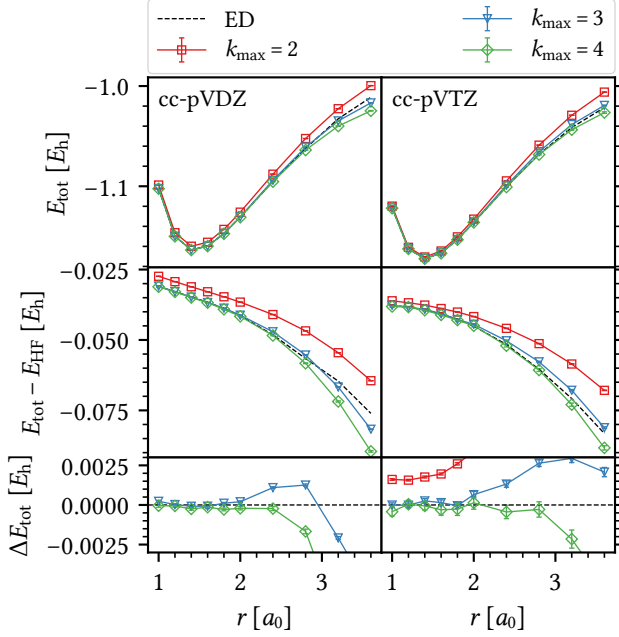


FIG. 11. Total energy E_{tot} with Monte Carlo errors for H_2 with cc-pVDZ (left column) and cc-pVTZ (right column) basis sets, $T = 50^{-1} E_h$. Top panels: comparison of ED and CDet at different k_{max} . Middle panel: total energy with Hartree-Fock contribution removed. Bottom panels: difference between ED and CDet.

higher as we go to a bigger basis for H_{10} . With cc-pVDZ, there are 50 atomic orbitals in total, with potential excitations to the empty orbitals from all 10 electrons. As shown in the right column Fig. 12, CDet still agrees with the reference method (MRCI+Q data from Ref. 59 at $T = 0$) for small values of r , but the Monte Carlo errors are significantly larger. Although our generic implementation has achieved decent extensibility without fine tuning for each specific system, more efficient Monte Carlo estimators and sampling schemes as well as analytical resummation techniques should advance the limit of CDet to more complex systems.

B. Analysis of computational cost

The computational cost of a Markov chain Monte Carlo simulation, measured as the computational time needed for reaching a result for observable X within a desired accuracy ΔX , is determined by three factors. First, the cost of each individual update, which is $O(k^3 2^k)$ for a configuration at expansion order k according to Algorithm 1. Second, the number of configuration updates needed to reach an independent sample by transversing a Markov chain of potentially correlated configurations, described by the integrated autocorrelation time τ_{int} . Finally, the variance $\text{Var}(X)$ of the estimator of the quan-

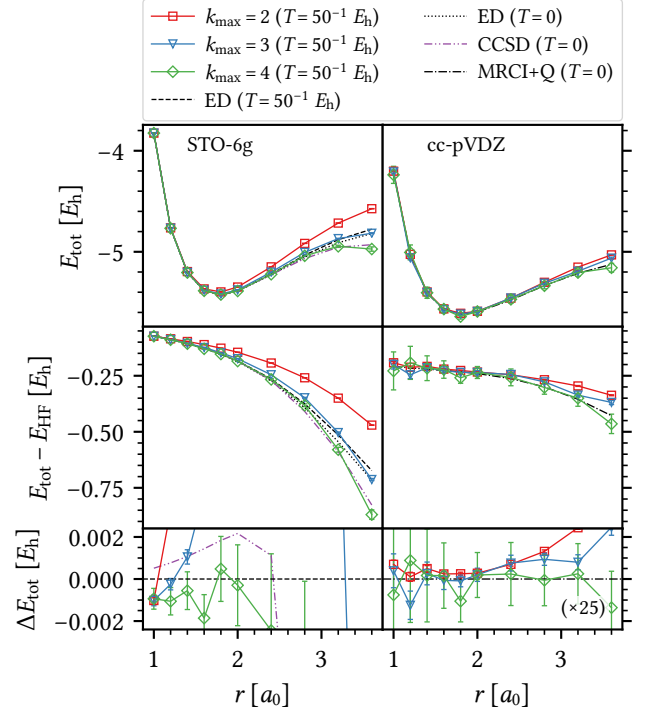


FIG. 12. Total energy E_{tot} with Monte Carlo errors for H_{10} with STO-6g (left column) and cc-pVDZ (right column) basis. ED results are used as reference for STO-6g and MRCI+Q ($T = 0$) from Ref. 59 for cc-pVDZ. Top panels: comparison of reference data and CDet at different k_{max} at finite temperature $T = 50^{-1} E_h$, along with ED and CCSD results at $T = 0$ for STO-6g basis. Middle panel: total energy with Hartree-Fock contribution removed. Bottom panels: difference between CDet and reference data at finite temperature, (for STO-6g) in comparison to difference between CCSD and ED at zero temperature.

tity of interest (Table I), such that

$$\Delta X = \sqrt{\frac{\text{Var}(X)}{N}} (2\tau_{\text{int}} + 1). \quad (64)$$

To assess the computational cost of our CDet implementation for reaching a certain uncertainty level, as well as how the effort changes with respect to temperature, choice of basis set, and system size, we perform a series of simulations of convergent series for the hydrogen chain H_n with the same Monte Carlo updates and measurements for a fixed number of Markov chain iterations. In Fig. 13, we show estimates of autocorrelation effects, actual computational costs, and stochastic uncertainties in total energy, as functions of temperature T , the number of orbitals N_{orb} , or the number of hydrogen atoms n in log-log plots. We rescale the y -values by an arbitrary factor to emphasize the respective scaling of these quantities in the same plot.

Figure 13.a shows the temperature dependence of CDet simulations of a fixed system (H_2 , STO-6g, $r =$

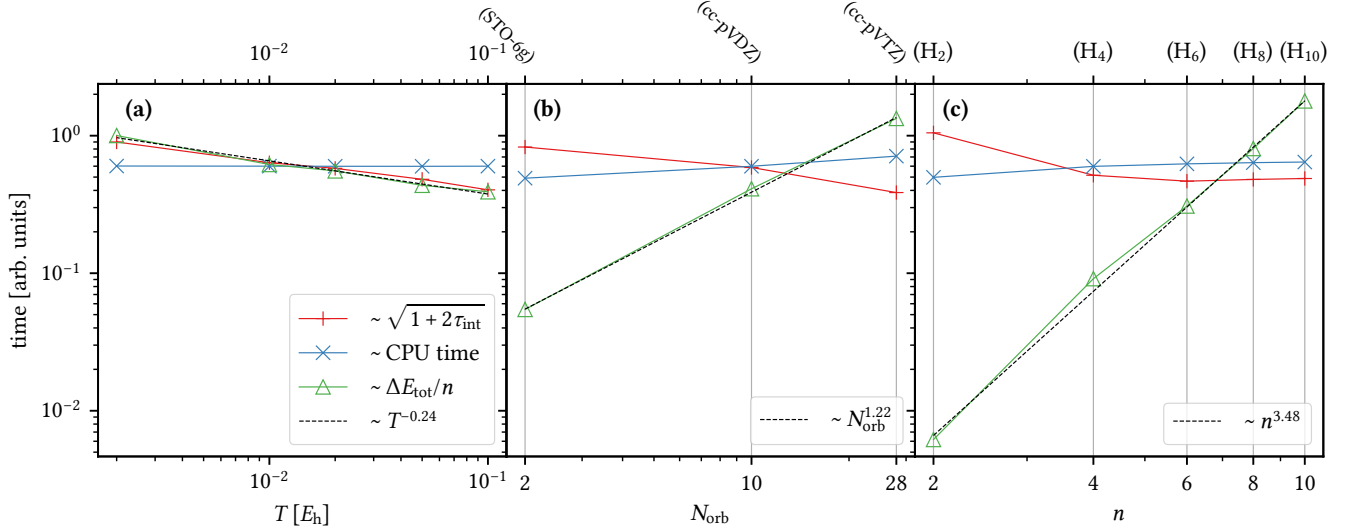


FIG. 13. Empirical cost analysis of CDet simulations of hydrogen chain H_n at $r = 1.4 a_0$. In each panel, all simulations are carried out using the same setup of Monte Carlo updates and number of iterations. We estimate the contribution of integrated autocorrelation time τ_{int} to the stochastic error (blue), the computational cost (orange), and the total stochastic uncertainty of energy ΔE_{tot} (green) for each simulation, and scale them to the same range on double-logarithmic plots. (a) Temperature dependence, H_2 , STO-6g, $k_{\text{max}} = 6$. (b) Basis set dependence, H_2 , $T = 50^{-1} E_h$, $k_{\text{max}} = 4$. (c) System size dependence, H_n , cc-pVDZ, $T = 50^{-1} E_h$, $k_{\text{max}} = 4$.

$1.4 a_0$) at $k_{\text{max}} = 6$. We observe that the simulation time does not change significantly as we decrease temperature, indicating similar distributions of the expansion order (usually tilted to the highest order). The error estimate in total energy follows almost the same tendency as the factor of the autocorrelation effect $\sqrt{2\tau_{\text{int}} + 1}$, indicating the underlying energy estimator does not have strong temperature dependence. The autocorrelation effect shows a slow power-law increase as temperature is lowered, implying that our Monte Carlo updates remain efficient at low temperature.

A similar analysis is shown in Fig. 13.b for the basis set dependence of the same system (H_2 , $r = 1.4 a_0$) at fixed temperature. We perform CDet simulations with $k_{\text{max}} = 4$ for basis sets STO-6g, cc-pVDZ, and cc-pVTZ, with 2, 10, and 28 atomic orbitals, respectively. As we add more ‘virtual’ orbitals to the system, the computational time increases slowly, and the autocorrelation time even decreases as the additional orbitals improve the connectivity of Monte Carlo configurations. However, the stochastic error shows a different trend from the autocorrelation effect and increases (a fit with a power law results in $\sim N_{\text{orb}}^{1.22}$), meaning that the additional orbitals introduce more diagrammatic configurations with alternating signs that lead to stronger Monte Carlo fluctuations.

As we increase the systems size in Fig. 13.c by adding more hydrogen atoms, the stochastic error (normalized by the system size n) at fixed computational time increases with a much larger power law than Fig. 13.b (fitted $\sim n^{3.48}$), while the autocorrelation time barely changes. This implies that adding electrons that con-

tribute to excitations near the Fermi level rapidly increases the complexity of the diagrammatics. The result is very different from the situation where additional basis states for the same number of electrons are added (Fig. 13.b).

The behavior illustrated in Fig. 13.c also differs from diagrammatic Monte Carlo applications with short-range or on-site interactions, which are formulated directly in the thermodynamic limit [47–49] and usually do not show strong scaling dependencies on system size. We suspect the difference is caused by the long range nature of the bare Coulomb interaction, which introduces significant non-local electronic correlations as the system size increases. In this case, the use of ‘bold’ (or ‘screened’) interactions instead of the bare Coulomb interactions, as performed in Ref. 59, may alleviate the problem. However, “bold” methods must deal with intrinsic issues of misconvergence to unphysical solutions [73]. Moreover, adapting such a method to the CDet framework requires further algorithmic development. This topic is under active development [55, 65].

Thus, through the empirical analysis above, we have shown that for convergent series, the computational cost of our CDet implementation is not very sensitive to changes in temperature or basis sets, but depends strongly on the size of the system, or more specifically, on the number of valence electrons directly participating in electron excitations.

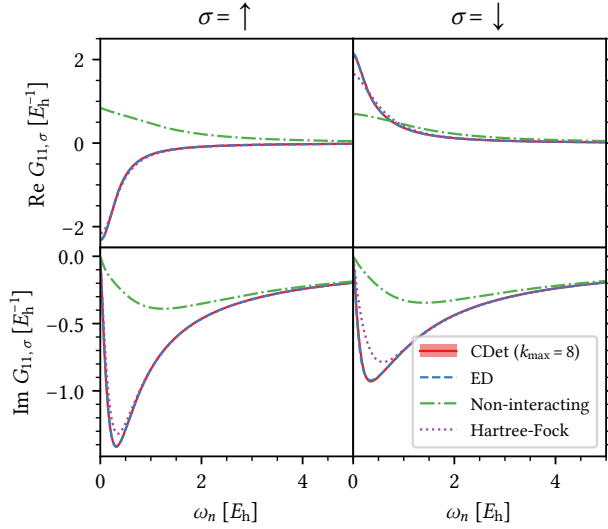


FIG. 14. Matsubara Green’s function for a NiO e_g impurity. Top (bottom) row shows the real (imaginary) part of the Green’s functions, and left (right) column shows values for spin up (down). Red solid lines: Impurity Green’s function from CDet with $k_{\max} = 8$. Monte Carlo error estimations are plotted as color shadings but smaller than line width. Blue dashed lines: Impurity Green’s function from ED, mostly overlapping with the CDet lines within line width. Green dash-dotted lines: ‘Non-interacting’ impurity propagator with discretized hybridization from ED. Purple dotted lines: Impurity Green’s function with Hartree-Fock counterterm as the starting point of CDet.

C. Realistic impurity: SEET for NiO

Finally, we test our CDet implementation in a general quantum impurity problem setup that includes the coupling to a non-interacting bath. We employ the SEET framework [23] for the antiferromagnetic compound NiO, which was studied by Mott [74] as one of the original correlated insulators. Following the computational setup in Ref. 58, we choose fcc NiO with lattice constant $a = 4.1705 \text{ \AA}$ at temperature $T \sim 451 \text{ K}$ ($\beta = 700 E_h^{-1}$). The unit cell is doubled along the [111] direction to capture the antiferromagnetic ordering, which contains two nickel atoms and two oxygen atoms. We use a $4 \times 4 \times 4$ momentum discretization and the gth-dzvp-molopt-sr basis set [75] with gth-pbe pseudopotential [76]. The Coulomb integral is decomposed using density fitting with the def2-svp-ri auxiliary basis [77]. For benchmark purposes, we select the e_g orbitals of both Ni atoms in the unit cell as the strongly correlated ‘impurities’, which is the minimal choice of impurities to capture correlation effects. This yields two independent impurities each with two orbitals. ‘Non-interacting’ impurity propagators are generated from a converged *GW* simulation of the complete unit cell following the SEET framework (for details of the computational setup see Ref. [58]).

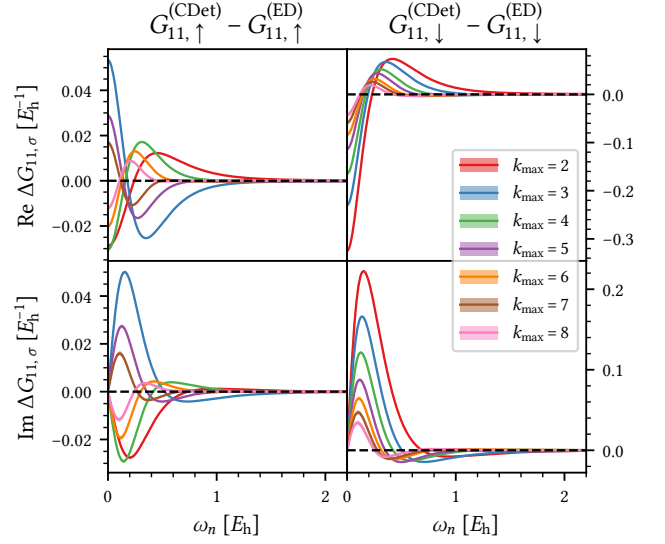


FIG. 15. Difference of CDet impurity Green’s functions to ED at different truncation order k_{\max} . Top (bottom) row shows the real (imaginary) part, and left (right) column shows values for spin up (down). Shadings indicate stochastic uncertainties of CDet.

As a benchmark, we compare our CDet impurity solver to the ED [78] results used in Ref. 58. ED requires the discretization of the continuous bath spectrum and its approximation by a few states. In order to separate ED bath fitting errors from the performance of the CDet method, we run our method for the ‘non-interacting’ impurity Green’s function g corresponding to the discretized non-interacting problem solved by ED. A precise listing of all parameters and input Green’s functions is given in the supplement [79]. Figure 14 shows the impurity Green’s functions for one of the two e_g impurities. At $k_{\max} = 8$, the impurity Green’s function from CDet agrees with the ED solution within line width, and the stochastic uncertainty is almost invisible. The spin polarization due to the antiferromagnetic ordering is greatly enhanced in both the ED and the CDet solutions, indicating that dynamical correlations plays an important role and are well captured by the selected impurity.

In Fig. 15, we take a closer look at the convergence of CDet series in comparison to ED by plotting the differences of CDet impurity Green’s functions to ED at different order truncations up to $k_{\max} = 8$. We observe that for both spins, the CDet result consistently converges to the ED result, giving agreement to within a percent for $k_{\max} = 8$. The convergence of the spin down component is slower than spin up, which is consistent to what can be observed in Fig. 14, i.e. the Hartree-Fock contribution already accounts for a greater part of the overall interaction contribution for the spin up component than for spin down.

The comparison to ED illustrates that our CDet solver can be reliably applied to general impurity problems as

part of a quantum embedding theory using the exact same framework as developed for molecules. We emphasize that, at the same complexity, systems with continuous bath states can be solved. Our method is therefore a controlled method for quantum impurities with general multi-orbital interactions and hybridizations, not limited by the systematic error introduced by the bath discretization procedure. The application of the solver to more complex impurities, where ED calculations are impractical, is a topic of subsequent publications.

IV. CONCLUSION

In conclusion, we have presented a diagrammatic Monte Carlo method for quantum impurity models with general interactions and hybridizations using the connected determinant formalism [52]. We have tested the method at the example of molecular systems, which presents a systematic way of changing correlation strength, system size, basis size, and temperature. We have also tested our method for impurity problems occurring in realistic quantum impurity calculations.

Our method is formulated in the language of Green's functions and self-energies. As a grand-canonical finite-temperature method, it is able to describe systems with particle number fluctuations and excited states. However, similar to other perturbative methods, the diagrammatic series breaks down in the strong correlation regime. This breakdown is clearly evident in the order-by-order convergence of the series and, as we have shown in detail, can be traced back to the pole structure of the diagram series.

Our method fills a crucial need of impurity solvers able to treat general four-fermion interaction and general off-diagonal hybridizations in large multi-orbital problem. It should therefore find applications in moderately correlated real-material simulations such as those occurring in DMFT [5, 6] and SEET [20–23].

Further methodological progress, such as the use of higher order counterterms [55], better integration methods [80], complex conformal mapping techniques [81–83], and other types of Monte Carlo updates will expand the accessible parameter regime of the method and may make simulations in the strongly correlated regime possible.

ACKNOWLEDGMENTS

JL, MW, and EG were supported by the Simons Foundation as part of the Simons Collaboration on the Many-Electron Problem. During the writing phase of the paper, MW was supported by the Austrian Science Fund (FWF) through the VeCoCo project (P30997). We thank Riccardo Rossi, Fedor Šimkovic, Félix Werner, and Dominika Zgid for helpful discussions. Molecular integrals are computed using the PYSCF library [84]. Exact di-

agonalization data are computed using the EDLIB library [78].

Appendix A: Hamiltonian

We describe the molecular electrons using the second quantized Hamiltonian

$$\hat{H} = \hat{H}_0 + \hat{H}_V, \quad (\text{A1a})$$

$$\hat{H}_0 = \sum_{pq} \sum_{\sigma} h_{pq} \hat{c}_{p\sigma}^{\dagger} \hat{c}_{q\sigma}, \quad (\text{A1b})$$

$$\hat{H}_V = \frac{1}{2} \sum_{pqrs} \sum_{\sigma\sigma'} V_{pqrs} \hat{c}_{p\sigma}^{\dagger} \hat{c}_{r\sigma'}^{\dagger} \hat{c}_{s\sigma'} \hat{c}_{q\sigma}, \quad (\text{A1c})$$

where $\hat{c}_{p\sigma}^{(\dagger)}$ is the electron annihilation (creation) operator associated with orbital ϕ_p and spin σ . The one- and two-body ‘matrix elements’ are defined as

$$h_{pq} = \int d\mathbf{r} \phi_p^*(\mathbf{r}) \left(-\frac{\nabla^2}{2m_e} - \sum_I^{N_n} \frac{Z_I}{|\mathbf{r} - \mathbf{R}_I|} \right) \phi_q(\mathbf{r}), \quad (\text{A2})$$

$$V_{pqrs} = \int d\mathbf{r} d\mathbf{r}' \phi_p^*(\mathbf{r}) \phi_q(\mathbf{r}) \frac{1}{|\mathbf{r} - \mathbf{r}'|} \phi_r^*(\mathbf{r}') \phi_s(\mathbf{r}'), \quad (\text{A3})$$

where $\{\mathbf{R}_I\}$ are the coordinates of the N_n nuclei, each with charge Z_I , and m_e is the electron mass. Eq. (A1) defines a quantum many-body problem which can be studied with a wide range of approximate or exact theoretical and numerical methods.

In order to combine spin and orbital indices in Eq. (A1), we introduce the compound notation $\{a, b, \dots\}$ such that

$$h_{ab} = h_{(p\sigma)(q\sigma')} \equiv h_{pq} \delta_{\sigma\sigma'} \quad (\text{A4})$$

$$V_{abcd} = V_{(p\sigma)(q\sigma')(r\lambda)(s\lambda')} \equiv V_{pqrs} \delta_{\sigma\sigma'} \delta_{\lambda\lambda'}. \quad (\text{A5})$$

The fermionic antisymmetry can be explicitly encoded in the anti-symmetrized interaction $U_{abcd} = V_{abcd} - V_{adcb}$, such that Eq. (A1) becomes

$$\hat{H}_0 + \hat{H}_V = \sum_{ab} h_{ab} \hat{c}_a^{\dagger} \hat{c}_b + \frac{1}{4} \sum_{abcd} U_{abcd} \hat{c}_a^{\dagger} \hat{c}_c^{\dagger} \hat{c}_d \hat{c}_b. \quad (\text{A6})$$

Appendix B: Scattering amplitude

The intuition in defining the M object is similar to the relation between the self-energy Σ and the Luttinger-Ward functional $\Phi[G]$

$$\Sigma(x', x) = \frac{\delta \Phi[G]}{\delta G(x, x')}, \quad (\text{B1})$$

which gives the 1PI amputated diagrams with the ‘bold’ propagator G [85]. Here we have employed the compound

space-time indices $x = (a, \tau)$. To get the connected amputated diagrams with the 'bare' propagator instead, we define a similar relation

$$M(x', x) = \beta \frac{\delta(\Omega - \Omega_0)}{\delta g(x, x')} = -\frac{\delta \log Z / Z_0}{\delta g(x, x')}. \quad (\text{B2})$$

We show that by carrying out this functional derivative, we will recover the definition of M as in Eq. (20).

Switching to the action formalism using coherent state path-integrals of Grassmann variables [61], we rewrite the partition function as

$$Z = \int \mathcal{D}[\bar{c}, c] e^{-S[\bar{c}, c]}, \quad (\text{B3})$$

where the action is given as

$$\begin{aligned} S &= S_0 + S_V, \\ S_0 &= - \int dy dy' \bar{c}(y') g^{-1}(y', y) c(y), \\ S_V &= \frac{1}{4} \int d\tau \sum_{abcd} U_{abcd} \bar{c}_a(\tau) \bar{c}_c(\tau) c_d(\tau) c_b(\tau). \end{aligned} \quad (\text{B4})$$

Observe that

$$\begin{aligned} \frac{\delta \log Z}{\delta g(x, x')} &= \frac{1}{Z} \frac{\delta}{\delta g(x, x')} \int \mathcal{D}[\bar{c}, c] \\ &\quad \times \exp \left[\int dy dy' \bar{c}(y') g^{-1}(y', y) c(y) - S_V \right] \\ &= \int dy dy' \frac{\delta g^{-1}(y', y)}{\delta g(x, x')} \frac{1}{Z} \int \mathcal{D}[\bar{c}, c] \bar{c}(y') c(y) e^{-S} \\ &= \int dy dy' \frac{\delta g^{-1}(y', y)}{\delta g(x, x')} G(y, y'). \end{aligned} \quad (\text{B5})$$

Using the fact that for an invertible matrix \mathbf{A} ,

$$(\mathbf{A} + \delta \mathbf{A})^{-1} - \mathbf{A}^{-1} = -\mathbf{A}^{-1} \delta \mathbf{A} \mathbf{A}^{-1} \quad (\text{B6})$$

$$\frac{\delta [\mathbf{A}^{-1}]_{ij}}{\delta \mathbf{A}_{kl}} = -[\mathbf{A}^{-1}]_{ik} [\mathbf{A}^{-1}]_{lj}, \quad (\text{B7})$$

we have

$$\frac{\delta \log Z}{\delta g(x, x')} = - \int dy dy' g^{-1}(x', y) G(y, y') g^{-1}(y', x). \quad (\text{B8})$$

Similarly in the non-interacting case,

$$\begin{aligned} \frac{\delta \log Z_0}{\delta g(x, x')} &= - \int dy dy' g^{-1}(x', y) g(y, y') g^{-1}(y', x) \\ &= -g^{-1}(x', x). \end{aligned} \quad (\text{B9})$$

Putting it all together, we have

$$\begin{aligned} M(x', x) &= -\frac{\delta \log(Z/Z_0)}{\delta g(x, x')} \\ &= \int dy dy' g^{-1}(x', y) [G(y, y') - g(y, y')] g^{-1}(y', x). \end{aligned} \quad (\text{B10})$$

Therefore

$$G(y, y') = g(y, y') + \int dx dx' g(y, x') M(x', x) g(x, y') \quad (\text{B11})$$

which is exactly the same as Eq. (20).

Expanding compound indices x, y, \dots , Eq. (B2) can be rewritten as

$$M_{ab}(\tau_1, \tau_2) = \beta \frac{\delta(\Omega - \Omega_0)}{\delta g_{ba}(\tau_2, \tau_1)}. \quad (\text{B12})$$

In practice, we usually work with the time-translational invariant functions $M(\tau)$ and $g(\tau)$ instead of their two-variable form. To that effect, we consider for $0 < \tau \leq \beta$,

$$\begin{aligned} \beta \frac{\delta(\Omega - \Omega_0)}{\delta g_{ba}(-\tau)} &= \sum_{a'b'} \int_0^\beta d\tau_1 d\tau_2 \frac{\beta \delta(\Omega - \Omega_0)}{\delta g_{b'a'}(\tau_2, \tau_1)} \frac{\delta g_{b'a'}(\tau_2, \tau_1)}{\delta g_{ba}(-\tau)} \\ &= \sum_{a'b'} \int_0^\beta d\tau_1 d\tau_2 M_{a'b'}(\tau_1 - \tau_2) \frac{\delta g_{b'a'}(\tau_2, \tau_1)}{\delta g_{ba}(-\tau)}, \end{aligned} \quad (\text{B13})$$

in which

$$\begin{aligned} \frac{\delta g_{b'a'}(\tau_2, \tau_1)}{\delta g_{ba}(-\tau)} &= \frac{\delta g_{b'a'}(\tau_2 - \tau_1)}{\delta g_{ba}(-\tau)} \\ &= \delta_{b'b} \delta_{a'a} [\delta(\tau_2 - \tau_1 + \tau) \Theta(\tau_1 - \tau_2) \\ &\quad - \delta(\tau_2 - \tau_1 + \tau - \beta) \Theta(\tau_2 - \tau_1)]. \end{aligned} \quad (\text{B14})$$

Therefore

$$\begin{aligned} \beta \frac{\delta(\Omega - \Omega_0)}{\delta g_{ba}(-\tau)} &= \sum_{a'b'} \int_0^\beta d\tau_1 d\tau_2 M_{a'b'}(\tau_1 - \tau_2) \\ &\quad \times \delta_{b'b} \delta_{a'a} [\delta(\tau_2 - \tau_1 + \tau) \Theta(\tau_1 - \tau_2) \\ &\quad - \delta(\tau_2 - \tau_1 + \tau - \beta) \Theta(\tau_2 - \tau_1)] \\ &= \int_0^\beta d\tau_1 d\tau_2 [M_{ab}(\tau) \delta(\tau_2 - \tau_1 + \tau) \Theta(\tau_1 - \tau_2) \\ &\quad - M_{ab}(\tau - \beta) \delta(\tau_2 - \tau_1 + \tau - \beta) \Theta(\tau_2 - \tau_1)] \\ &= M_{ab}(\tau) \int_0^\beta d\tau_1 d\tau_2 [\delta(\tau_2 - \tau_1 + \tau) \Theta(\tau_1 - \tau_2) \\ &\quad + \delta(\tau_2 - \tau_1 + \tau - \beta) \Theta(\tau_2 - \tau_1)] \\ &= M_{ab}(\tau) \int_0^\beta d\tau_1 \int_{\tau_1}^{\tau_1 + \beta} d\tau_2 \delta(\tau_2 - \tau_1 + \tau - \beta) \\ &= \beta M_{ab}(\tau), \end{aligned} \quad (\text{B15})$$

which gives Eq. (21).

Appendix C: Thermal expectation value of the electron energy

The one-body energy is straightforward:

$$E_0 = \langle \hat{H}_0 \rangle = \sum_{ab} h_{ab} \langle \hat{c}_a^\dagger \hat{c}_b \rangle = \sum_{ab} h_{ab} \rho_{ab}. \quad (\text{C1})$$

Expression for the two-body energy term can be derived in multiple ways such as using the equation of motion or the Schwinger-Dyson equation. Here we provide a simple derivation following Ref. 86. We introduce a coupling constant ξ to the action defined in Eq. (B4) such that $S_\xi = S_0 + \xi S_V$ and $\xi \rightarrow 1$ recovers the ‘physical’ results. Now we have

$$\begin{aligned} \left. \frac{dZ_\xi}{d\xi} \right|_{\xi=1} &= - \int \mathcal{D}[\bar{c}, c] S_V e^{-S_0 - \xi S_V} \Big|_{\xi=1} \\ &= -Z \left\langle \int_0^\beta d\tau \frac{U_{abcd}}{4} \bar{c}_a(\tau) \bar{c}_c(\tau) c_d(\tau) c_b(\tau) \right\rangle \\ &= -Z\beta \langle \hat{H}_V \rangle. \end{aligned} \quad (\text{C2})$$

Introducing a change of variables such that $c \rightarrow c/\xi^{1/4}$ and $\bar{c} \rightarrow \bar{c}/\xi^{1/4}$, then

$$\begin{aligned} \mathcal{D}[\bar{c}, c] &= \lim_{\mathcal{N} \rightarrow \infty} \prod_{\alpha=1}^{\mathcal{N}} d\bar{c}_\alpha dc_\alpha \\ &\rightarrow \lim_{\mathcal{N} \rightarrow \infty} \xi^{+\mathcal{N}/2} \prod_{\alpha=1}^{\mathcal{N}} d\bar{c}_\alpha dc_\alpha \\ &= \lim_{\mathcal{N} \rightarrow \infty} \xi^{+\text{Tr}[I]/2} \prod_{\alpha=1}^{\mathcal{N}} d\bar{c}_\alpha dc_\alpha \\ &= \xi^{+\text{Tr}[I]/2} \mathcal{D}[\bar{c}, c] \end{aligned} \quad (\text{C3})$$

where the indices α denote states at each discretized time point on the integration path, $\text{Tr}[I] = \int dx \delta(x, x)$ in which x is the compound spacetime index, and the plus sign on the exponent is due to the nature of Grassmann integrals. The partition function is unaffected by the change of variables, which now takes the form

$$Z_\xi = \xi^{\text{Tr}[I]/2} \int \mathcal{D}[\bar{c}, c] e^{-\xi^{-1/2} S_0 - S_V}. \quad (\text{C4})$$

Therefore

$$\begin{aligned} \left. \frac{dZ_\xi}{d\xi} \right|_{\xi=1} &= \frac{\text{Tr}[I]}{2} Z + \int \mathcal{D}[\bar{c}, c] \frac{\xi^{-3/2}}{2} S_0 e^{-\xi^{-1/2} S_0 - S_V} \Big|_{\xi=1} \\ &= \frac{\text{Tr}[I]}{2} Z - \frac{1}{2} \int \mathcal{D}[\bar{c}, c] g^{-1}(x', x) \bar{c}(x') c(x) e^{-S} \\ &= \frac{\text{Tr}[I]}{2} Z - \frac{Z}{2} g^{-1}(x', x) G(x, x') \\ &= \frac{Z}{2} \text{Tr}[I - g^{-1}G] \end{aligned} \quad (\text{C5})$$

Comparing (C2) and (C5), we have

$$\begin{aligned} \langle \hat{H}_V \rangle &= \frac{1}{2\beta} \text{Tr}[g^{-1}G - I] = \frac{1}{2\beta} \text{Tr}[(g^{-1} - G^{-1})G] \\ &= \frac{1}{2\beta} \text{Tr}[\Sigma G] \end{aligned} \quad (\text{C6})$$

Appendix D: Recursion relations for the grand potential

The expansion of the grand potential, Eq. (16), consists of connected vacuum diagrams as shown in Fig. 1. As a result of Wick’s theorem (10), all vacuum diagrams $D(\mathcal{V})$ for a fixed vertex configuration \mathcal{V} can be partitioned into a connected subdiagram and the remainder of the vacuum components. Since no external legs exist to serve as reference points for defining connectivity, we start by picking a specific vertex $v \in \mathcal{V}$ as the ‘reference’ and consider connectivity with respect to v , i.e.

$$D(\mathcal{V}) = \sum_{\substack{\mathcal{S} \subseteq \mathcal{V} \\ \mathcal{S} \ni v}} D_c(\mathcal{S}) D(\mathcal{V} \setminus \mathcal{S}). \quad (\text{D1})$$

As the choice of v is arbitrary, it can be any of the $k = |\mathcal{V}|$ vertices in \mathcal{V} , therefore

$$D(\mathcal{V}) = \frac{1}{|\mathcal{V}|} \sum_{v \in \mathcal{V}} \sum_{\substack{\mathcal{S} \subseteq \mathcal{V} \\ \mathcal{S} \ni v}} D_c(\mathcal{S}) D(\mathcal{V} \setminus \mathcal{S}). \quad (\text{D2})$$

This is equivalent to iterating all possible subsets \mathcal{S} of \mathcal{V} where the reference v can be any vertex in \mathcal{S} :

$$\begin{aligned} D(\mathcal{V}) &= \frac{1}{|\mathcal{V}|} \sum_{\mathcal{S} \subseteq \mathcal{V}} \sum_{v \in \mathcal{S}} D_c(\mathcal{S}) D(\mathcal{V} \setminus \mathcal{S}) \\ &= \sum_{\mathcal{S} \subseteq \mathcal{V}} \frac{|\mathcal{S}|}{|\mathcal{V}|} D_c(\mathcal{S}) D(\mathcal{V} \setminus \mathcal{S}). \end{aligned} \quad (\text{D3})$$

We now extract the term where $\mathcal{S} = \mathcal{V}$ from the right hand side and obtain the recursive formula for $D_c(\mathcal{V})$:

$$D_c(\mathcal{V}) = D(\mathcal{V}) - \sum_{\mathcal{S} \subsetneq \mathcal{V}} \frac{|\mathcal{S}|}{|\mathcal{V}|} D_c(\mathcal{S}) D(\mathcal{V} \setminus \mathcal{S}). \quad (\text{D4})$$

The initial condition is the zeroth order contribution $D_c(\emptyset) = 0$.

A more general framework of deriving the recursion relations using idempotent polynomials is described in Ref. 53. This framework does not resort to topological arguments.

Appendix E: Numerical computation of the adjugate matrix

We calculate the adjugate $\text{adj}(A)$ of a matrix $A \in \mathbb{R}^{n \times n}$ numerically by first performing a rank-revealing factorization on the matrix [87], such as the pivoted QR via the Householder algorithm

$$A = QDRP \quad (\text{E1})$$

where Q is an orthogonal matrix of Householder reflections, D is a diagonal matrix, R is an upper triangular matrix in which all diagonal elements equal 1, and P is a

permutation matrix of the columns. The rank of the matrix $r = \text{rank}(A)$ is determined by the number of nonzero diagonal elements of D .

If A is not singular, i.e. $r = n$, then the adjugate is given by

$$\begin{aligned} \text{adj}(A) &= \det(A)A^{-1} \\ &= \det(P)\det(D)\det(Q)P^T R^{-1}D^{-1}Q^T \\ &= \left[(-1)^{n_P n_Q} \prod_{i=1}^n d_i\right] P^T R^{-1}D^{-1}Q^T, \end{aligned} \quad (\text{E2})$$

where n_P is the number of transpositions in the permutation P , n_Q is the number of Householder reflections in Q , and d_i are diagonal elements of D . The scaling as a function of n for the complexity of calculating the adjugate is the same as the one for calculating A^{-1} , and we obtain $\det(A)$ at the same time.

If A is singular, i.e. $r < n$, $\det(A)$ becomes zero, and Eq. (E2) is replaced by

$$\text{adj}(A) = \left[(-1)^{n_P n_Q} \prod_{i=1}^n d_i\right] P^T R^{-1} \text{adj}(D) Q^T. \quad (\text{E3})$$

If $r = n - 1$, there is one zero in the diagonal of D . Assuming $d_n = 0$ and $d_i \neq 0$ for $i = 1, \dots, n - 1$, the adjugate of D follows directly from the definition (23)

$$\text{adj}(D) = \text{diag}\left(\left[0, \dots, 0, \prod_{i=1}^{n-1} d_i\right]\right). \quad (\text{E4})$$

If $r < n - 1$, $\text{adj}(D) = 0$, therefore $\text{adj}(A) = 0$.

In the presence of off-diagonal propagators, it is possible that the amputated diagrams $\mathbf{A}(\mathcal{V})$ is nonzero while the vacuum diagrams $D(\mathcal{V}, \emptyset)$ vanish. Therefore it is crucial to implement the adjugate of singular matrices as discussed above.

-
- [1] P. W. Anderson, Phys. Rev. **124**, 41 (1961).
 - [2] R. Hanson, L. P. Kouwenhoven, J. R. Petta, S. Tarucha, and L. M. K. Vandersypen, Reviews of Modern Physics **79**, 1217 (2007).
 - [3] R. Brako and D. M. Newns, Journal of Physics C: Solid State Physics **14**, 3065 (1981).
 - [4] D. C. Langreth and P. Nordlander, Phys. Rev. B **43**, 2541 (1991).
 - [5] A. Georges, G. Kotliar, W. Krauth, and M. J. Rozenberg, Reviews of Modern Physics **68**, 13 (1996).
 - [6] G. Kotliar, S. Y. Savrasov, K. Haule, V. S. Oudovenko, O. Parcollet, and C. A. Marianetti, Reviews of Modern Physics **78**, 865 (2006).
 - [7] A. I. Lichtenstein and M. I. Katsnelson, Phys. Rev. B **62**, R9283(R) (2000).
 - [8] G. Kotliar, S. Y. Savrasov, G. Pálsson, and G. Biroli, Phys. Rev. Lett. **87**, 186401 (2001).
 - [9] M. H. Hettler, M. Mukherjee, M. Jarrell, and H. R. Krishnamurthy, Phys. Rev. B **61**, 12739 (2000).
 - [10] T. Maier, M. Jarrell, T. Pruschke, and M. H. Hettler, Rev. Mod. Phys. **77**, 1027 (2005).
 - [11] V. I. Anisimov, A. I. Poteryaev, M. A. Korotin, A. O. Anokhin, and G. Kotliar, Journal of Physics: Condensed Matter **9**, 7359 (1997).
 - [12] A. I. Lichtenstein and M. I. Katsnelson, Physical Review B **57**, 6884 (1998).
 - [13] K. Held, I. A. Nekrasov, G. Keller, V. Eyert, N. Blümer, A. K. McMahan, R. T. Scalettar, T. Pruschke, V. I. Anisimov, and D. Vollhardt, physica status solidi (b) **243**, 2599 (2006).
 - [14] P. Sun and G. Kotliar, Physical Review B **66**, 085120 (2002).
 - [15] S. Biermann, F. Aryasetiawan, and A. Georges, Physical Review Letters **90**, 086402 (2003).
 - [16] S. Biermann, F. Aryasetiawan, and A. Georges, in *Physics of Spin in Solids: Materials, Methods and Applications*, edited by S. Halilov (Springer Netherlands, Dordrecht, 2005) pp. 43–65.
 - [17] L. Boehnke, F. Nilsson, F. Aryasetiawan, and P. Werner, Physical Review B **94**, 201106(R) (2016).
 - [18] S. Choi, A. Kutepov, K. Haule, M. van Schilfgaarde, and G. Kotliar, npj Quantum Materials **1**, 16001 (2016).
 - [19] J. Lee and K. Haule, Phys. Rev. B **95**, 155104 (2017).
 - [20] A. A. Kananenka, E. Gull, and D. Zgid, Physical Review B **91**, 121111(R) (2015).
 - [21] T. N. Lan, A. A. Kananenka, and D. Zgid, The Journal of Chemical Physics **143**, 241102 (2015).
 - [22] T. N. Lan, A. A. Kananenka, and D. Zgid, Journal of Chemical Theory and Computation **12**, 4856 (2016).
 - [23] D. Zgid and E. Gull, New Journal of Physics **19**, 023047 (2017).
 - [24] V. V. Mazurenko, S. N. Isakov, A. N. Rudenko, V. I. Anisimov, and A. I. Lichtenstein, Phys. Rev. B **82**, 193403 (2010).
 - [25] M. Caffarel and W. Krauth, Phys. Rev. Lett. **72**, 1545 (1994).
 - [26] M. Capone, M. Civelli, S. S. Kancharla, C. Castellani, and G. Kotliar, Phys. Rev. B **69**, 195105 (2004).
 - [27] E. Koch, G. Sangiovanni, and O. Gunnarsson, Phys. Rev. B **78**, 115102 (2008).
 - [28] A. Liebsch and N.-H. Tong, Phys. Rev. B **80**, 165126 (2009).
 - [29] D. Sénéchal, Phys. Rev. B **81**, 235125 (2010).
 - [30] Y. Lu, M. Höppner, O. Gunnarsson, and M. W. Haverkort, Phys. Rev. B **90**, 085102 (2014).
 - [31] D. Zgid, E. Gull, and G. K.-L. Chan, Phys. Rev. B **86**, 165128 (2012).
 - [32] A. Shee and D. Zgid, Journal of Chemical Theory and Computation **15**, 6010 (2019), pMID: 31518129.
 - [33] T. Zhu, C. A. Jiménez-Hoyos, J. McClain, T. C. Berkelbach, and G. K.-L. Chan, Phys. Rev. B **100**, 115154 (2019).
 - [34] A. Weichselbaum and J. von Delft, Phys. Rev. Lett. **99**, 076402 (2007).
 - [35] R. Bulla, T. A. Costi, and T. Pruschke, Rev. Mod. Phys. **80**, 395 (2008).

- [36] E. Gull, A. J. Millis, A. I. Lichtenstein, A. N. Rubtsov, M. Troyer, and P. Werner, *Reviews of Modern Physics* **83**, 349 (2011).
- [37] A. N. Rubtsov, V. V. Savkin, and A. I. Lichtenstein, *Physical Review B* **72**, 035122 (2005).
- [38] E. Gull, P. Werner, O. Parcollet, and M. Troyer, *EPL (Europhysics Letters)* **82**, 57003 (2008).
- [39] E. Gull, P. Staar, S. Fuchs, P. Nukala, M. S. Summers, T. Pruschke, T. C. Schulthess, and T. Maier, *Phys. Rev. B* **83**, 075122 (2011).
- [40] J. P. F. LeBlanc, A. E. Antipov, F. Becca, I. W. Bulik, G. K.-L. Chan, C.-M. Chung, Y. Deng, M. Ferrero, T. M. Henderson, C. A. Jiménez-Hoyos, E. Kozik, X.-W. Liu, A. J. Millis, N. V. Prokof'ev, M. Qin, G. E. Scuseria, H. Shi, B. V. Svistunov, L. F. Tocchio, I. S. Tupitsyn, S. R. White, S. Zhang, B.-X. Zheng, Z. Zhu, and E. Gull (Simons Collaboration on the Many-Electron Problem), *Phys. Rev. X* **5**, 041041 (2015).
- [41] E. Gorelov, T. O. Wehling, A. N. Rubtsov, M. I. Katsnelson, and A. I. Lichtenstein, *Phys. Rev. B* **80**, 155132 (2009).
- [42] P. Werner, A. Comanac, L. de' Medici, M. Troyer, and A. J. Millis, *Phys. Rev. Lett.* **97**, 076405 (2006).
- [43] P. Werner and A. J. Millis, *Phys. Rev. B* **74**, 155107 (2006).
- [44] K. Haule, *Phys. Rev. B* **75**, 155113 (2007).
- [45] E. Eidelstein, E. Gull, and G. Cohen, *arXiv:1907.08570 [cond-mat.str-el]* (2019).
- [46] G. Cohen, E. Gull, D. R. Reichman, and A. J. Millis, *Phys. Rev. Lett.* **115**, 266802 (2015).
- [47] N. V. Prokof'ev and B. V. Svistunov, *Physical Review Letters* **81**, 2514 (1998).
- [48] N. Prokof'ev and B. Svistunov, *Physical Review B* **77**, 020408(R) (2008).
- [49] N. V. Prokof'ev and B. V. Svistunov, *Physical Review B* **77**, 125101 (2008).
- [50] K. van Houcke, E. Kozik, N. Prokof'ev, and B. Svistunov, *Physics Procedia* **6**, 95 (2010), computer Simulations Studies in Condensed Matter Physics XXI.
- [51] K. Chen and K. Haule, *Nature Communications* **10**, 3725 (2019).
- [52] R. Rossi, *Physical Review Letters* **119**, 045701 (2017).
- [53] R. Rossi, *arXiv:1802.04743 [cond-mat.str-el]* (2018).
- [54] A. Boag, E. Gull, and G. Cohen, *Phys. Rev. B* **98**, 115152 (2018).
- [55] R. Rossi, F. Simkovic, and M. Ferrero, *arXiv:2001.09133 [cond-mat.str-el]* (2020).
- [56] A. Moutenet, W. Wu, and M. Ferrero, *Physical Review B* **97**, 085117 (2018).
- [57] F. Šimkovic and E. Kozik, *Physical Review B* **100**, 121102 (2019).
- [58] S. Isakov, C.-N. Yeh, E. Gull, and D. Zgid, *Ab-initio self-energy embedding for the photoemission spectra of nio and mno* (2020), *arXiv:2003.04440 [cond-mat.str-el]*.
- [59] M. Motta, D. M. Ceperley, G. K.-L. Chan, J. A. Gomez, E. Gull, S. Guo, C. A. Jiménez-Hoyos, T. N. Lan, J. Li, F. Ma, A. J. Millis, N. V. Prokof'ev, U. Ray, G. E. Scuseria, S. Sorella, E. M. Stoudenmire, Q. Sun, I. S. Tupitsyn, S. R. White, D. Zgid, and S. Zhang, *Physical Review X* **7**, 031059 (2017).
- [60] A. A. Abrikosov, L. P. Gorkov, and I. Y. Dzyaloshinskii, *Methods of Quantum Field Theory in Statistical Physics* (Pergamon, 1965).
- [61] J. W. Negele and H. Orland, *Quantum Many-particle Systems* (Addison-Wesley, 1988).
- [62] Rossi, R., Prokof'ev, N., Svistunov, B., Van Houcke, K., and Werner, F., *EPL* **118**, 10004 (2017).
- [63] C. Bertrand, O. Parcollet, A. Maillard, and X. Waintal, *Phys. Rev. B* **100**, 125129 (2019).
- [64] P. Gunacker, M. Wallerberger, E. Gull, A. Hausoel, G. Sangiovanni, and K. Held, *Phys. Rev. B* **92**, 155102 (2015).
- [65] R. Rossi, F. Werner, N. V. Prokof'ev, and B. Svistunov, *Physical Review B* **93**, 161102(R) (2016).
- [66] W. J. Hehre, R. F. Stewart, and J. A. Pople, *The Journal of Chemical Physics* **51**, 2657 (1969).
- [67] A. Szabo and N. S. Ostlund, *Modern quantum chemistry: introduction to advanced electronic structure theory* (Courier Corporation, 2012).
- [68] P. Knowles, K. Somasundram, N. Handy, and K. Hirao, *Chemical Physics Letters* **113**, 8 (1985).
- [69] J. Olsen, O. Christiansen, H. Koch, and P. Jørgensen, *Journal of Chemical Physics* **105**, 5082 (1996).
- [70] S. Hirata, M. R. Hermes, J. Simons, and J. V. Ortiz, *Journal of Chemical Theory and Computation* **11**, 1595 (2015).
- [71] S. Hirata, A. E. Doran, P. J. Knowles, and J. V. Ortiz, *The Journal of Chemical Physics* **147**, 044108 (2017).
- [72] Z. Li, *The Journal of Chemical Physics* **151**, 244114 (2019).
- [73] E. Kozik, M. Ferrero, and A. Georges, *Phys. Rev. Lett.* **114**, 156402 (2015).
- [74] N. F. Mott, *Proceedings of the Physical Society. Section A* **62**, 416 (1949).
- [75] J. VandeVondele and J. Hutter, *The Journal of Chemical Physics* **127**, 114105 (2007).
- [76] S. Goedecker, M. Teter, and J. Hutter, *Phys. Rev. B* **54**, 1703 (1996).
- [77] C. Hättig, *Phys. Chem. Chem. Phys.* **7**, 59 (2005).
- [78] S. Isakov and M. Danilov, *Computer Physics Communications* **225**, 128 (2018).
- [79] See Supplemental Material at [URL will be inserted by publisher] for a precise listing of the input 'non-interacting' Green's function g (without Hartree-Fock contribution) and the interaction tensor V defined in Appendix A. Data is stored as a comma-separated text file with explanatory headers and comments.
- [80] M. Maček, P. T. Dumitrescu, C. Bertrand, B. Triggs, O. Parcollet, and X. Waintal, *arXiv:2002.12372 [cond-mat.str-el]* (2020).
- [81] W. Wu, M. Ferrero, A. Georges, and E. Kozik, *Phys. Rev. B* **96**, 041105 (2017).
- [82] R. Rossi, T. Ohgoe, K. van Houcke, and F. Werner, *Phys. Rev. Lett.* **121**, 130405 (2018).
- [83] C. Bertrand, S. Florens, O. Parcollet, and X. Waintal, *Phys. Rev. X* **9**, 041008 (2019).
- [84] Q. Sun, T. C. Berkelbach, N. S. Blunt, G. H. Booth, S. Guo, Z. Li, J. Liu, J. D. McClain, E. R. Sayfutyarova, S. Sharma, S. Wouters, and G. K. L. Chan, *Wiley Interdisciplinary Reviews: Computational Molecular Science* **8**, e1340 (2018).
- [85] J. M. Luttinger and J. C. Ward, *Phys. Rev.* **118**, 1417 (1960).
- [86] L. Lin and M. Lindsey, *arXiv:1809.02900* (2018).
- [87] G. W. Stewart, *Linear Algebra and its Applications* **283**, 151 (1998).